Journal of Computational Physics 229 (2010) 958–977

Contents lists available at ScienceDirect

Journal of Computational Physics

journal homepage: www.elsevier.com/locate/jcp

Modeling simple locomotors in Stokes flow

Alex Kanevsky [a,*], Michael J. Shelley [a], Anna-Karin Tornberg [a,b]

[a] Courant Institute of Mathematical Sciences, New York University, 251 Mercer Street, New York, NY 10012, United States
[b] Royal Institute of Technology (KTH), Numerical Analysis/Linne' Flow Center, SE-100 44 Stockholm, Sweden

ARTICLE INFO

Article history:
Received 27 February 2008
Received in revised form 9 March 2009
Accepted 15 May 2009
Available online 27 May 2009

Keywords:
Stokes equations
Boundary integral formulation
Nystrom collocation
Locomotors

ABSTRACT

Motivated by the locomotion of flagellated micro-organisms and by recent experiments of chemically driven nanomachines, we study the dynamics of bodies of simple geometric shape that are propelled by specified tangential surface stresses. We develop a mathematical description of the body dynamics based on a mixed-type boundary integral formulation. We also derive analytic axisymmetric solutions for the case of a single locomoting sphere and ellipsoid based on spherical and ellipsoidal harmonics, and compare our numerical results to these. The hydrodynamic interactions between two spherical and ellipsoidal swimmers in an infinite fluid are then simulated using second-order accurate spatial and temporal discretizations. We find that the near-field interactions result in complex and interesting changes in the locomotors' orientations and trajectories. Stable as well as unstable pairwise swimming motions are observed, similar to the recent findings of Pooley et al. [C.M. Pooley, G.P. Alexander, J.M. Yeomans, Hydrodynamic interaction between two swimmers at low Reynolds number, Phys. Rev. Lett. 99 (2007) 228103].

1. Introduction

A fascinating, important, and counter-intuitive fluid dynamic world exists and thrives at length scales that are difficult for the human eye to see. In this micro and nano-scale empire, the Reynolds number $\mathrm{Re} = \rho UL/\mu \ll 1$ (ρ is the density of the fluid, U is a characteristic velocity, L is a characteristic length, and μ is the fluid viscosity) is very small, viscous forces are dominant, inertial forces are negligible, time is irrelevant, and geometric configuration trumps all. For a beautiful introduction, see the article by Purcell [20]. A zero Reynolds number assumption is a good approximation to the low-Re dynamics, leading to the simplification of the nonlinear, time-dependent Navier–Stokes partial differential equations that govern general continuous fluid flows, to the linear incompressible Stokes equations [19,7,1]

$$-\nabla p + \mu\nabla^2\mathbf{u} = 0, \quad \nabla\cdot\mathbf{u} = 0, \tag{1}$$

where $\mathbf{u}$ is the flow velocity field, p is the pressure, and $\nabla\cdot\mathbf{u} = 0$ is the equation of continuity for incompressible flows.

Examples of motion in a Stokes flow – described by Eq. (1) – are ubiquitous in Nature and numerous examples may be found in the biological world. The coordinated activity of motile spermatozoa, which propel themselves by beating a flagellum in a nonreciprocal three-dimensional pattern, is an essential ingredient for mammalian fertilization and reproduction [5]. The motile bacteria *Escherichia coli* (*E. coli*) is frequently used as a model organism in microbiology studies [2], and is commonly found in the lower intestine of warm-blooded animals, and may lead to various infections and diseases in the host. Aquatic micro-organisms such as phytoplankton play an important role in oceanic ecosystems as well as the global climate. Phytoplankton provide a critical food source for larger animals ranging from zooplankton to whales, and also absorb CO_2 from the water which originates in the atmosphere.

* Corresponding author.
E-mail address: kanevsky@cims.nyu.edu (A. Kanevsky).

0021-9991/$ - see front matter © 2009 Elsevier Inc. All rights reserved.
doi:10.1016/j.jcp.2009.05.030

Nanotechnology is yet another field where Stokes flows are important. One of the current challenges in nanotechnology is to create miniature engines that can convert stored chemical energy to motion. Experiments carried out in [17] are a step in this direction, in which Paxton et al. synthesized and demonstrated autonomously moving nanoparticle locomotors. These "chemical" locomotors are cylindrical nanorods 2 μm long and 370 nm in diameter, half of which is coated with gold, while the other half is coated with platinum. The asymmetry is essential, since Pt (platinum) is an active hydrogen peroxide decomposition catalyst. The rods move mainly along their axis at average speeds of 8 μm/s autonomously in aqueous hydrogen peroxide solutions by catalyzing formation of oxygen at the Pt end, and exhibit dynamics very similar to those of motile organisms.

The literature is rich on the mathematical analysis, modeling and numerical simulation of bodies in Stokes flows sedimenting passively in gravitational fields. For example, Stimson and Jeffrey [29] solved the problem of two spheres falling parallel to their line-of-centers in a viscous fluid, while Goldman et al. [6] solved the more general problem of two spheres falling that are oriented at an arbitrary angle with respect to their line-of- centers. Recently, Tornberg and Shelley [32,24,30], Tornberg and Gustavsson [31], and Saintillan et al. [22] developed state-of-the-art boundary integral methods for simulating the dynamics of multiple interacting slender flexible and rigid fibers suspended in fluids. There are also many examples for non-slender bodies (see [4] for a review).

There have been far fewer experimental or numerical investigations of active swimmers in Stokes flow. Part of the reason for this is the level of difficulty and the degree of sophistication associated in performing experiments with active swimmers. However, there have recently been several very interesting experimental/theoretical studies of motile bodies. Solari et al. [28] studied the motility and molecular transport of flagellated colonial organisms, such as the volvocalean green algae *Volvox carteri*. Using particle image velocimetry (PIV), they measured the velocity field surrounding *V. carteri* colonies that were held fixed in place, and observed that the velocity field in very close proximity to the body of the *Volvox* is not zero due to the action of the flagella, which are used to propel the organism.

In subsequent work, Short et al. [25] showed that the beating of flagella by an organism such as *V. carteri* not only confers it motility, but also plays a crucial role in its viability. They introduced a model that assumes that a swimmer exerts a constant tangential stress along its surface, which has strongly influenced our work here. According to their model, flow velocity grows linearly with colony radius, which results in colony swimming speeds close to experimentally observed values. For spherical organisms, the required nutrient transport rate grows quadratically with radius, and thus cannot be satisfied by purely diffusive transport processes (which grow linearly with the radius). The model in [25] predicts that the flow-field generated by flagella-driven stirring results in an advective transport process which is quadratic in the radius, thus enhancing the nutrient uptake rate (metabolite exchange rate per unit area) of a colony and overcoming the size barrier (bottleneck radius) that would result from purely diffusive transport. Furthermore, they measured actual flow-fields for *V. carteri* to confirm their analysis experimentally. They demonstrated that at least one advantage of increased size is a greater nutrient acquisition rate.

Related low-Reynolds number fluid dynamical models have been developed over past decades for various actively swimming micro-organisms. The "squirmer" model was introduced by Lighthill [14], and extended by Blake [3], Magar et al. [15], and Magar and Pedley [16]. The squirmer is a spherical locomotor with a prescribed tangential surface velocity. Ishikawa et al. [13] calculated and investigated the fluid-dynamical interaction of two model squirmers, and Ishikawa and Hota [8] applied the squirmer model to compute the hydrodynamic interaction of two paramecia. Furthermore, the rheology, diffusion, and orientational relaxation time of semi-dilute suspensions of squirmers were studied by Ishikawa et al. in [9–11]. Saintillan and Shelley [23] developed a model based on slender-body theory for slender rodlike swimmers that exert a tangential shear stress on the fluid over part of their bodies, and found theoretically predicted instabilities [27] in their simulations of suspensions of self-locomoting particles that had an initial long-range orientational order, as well as large-scale flows and mixing and persistence of short-range orientational order.

Motivated by the locomotion of flagellated micro-organisms and by recent experiments of chemically driven nanomachines, we develop a particular model to study the dynamics of bodies of simple geometric shape that are propelled by surface stresses. As in previous models [15,25], the body and the flagella are treated as a smooth envelope, and all points on the surface are assumed to impart a motive tangential stress on the surrounding fluid in the motive direction, thus continuously displacing fluid along the surface in that same direction. This generalizes the model of Short et al. [25] by allowing for inhomogenous motive tangential stress, nonspherical bodies, and body-body interactions. In this model, after specifying the motive stress, a surface slip velocity is determined, relative to an overall body translation and rotation, as is the surface normal stress, and the tangential stress component normal to the motive part. Body-body interactions do influence the magnitude of the relative slip velocity, as well as contribute to the overall translation and rotation, but they do not change its direction. Furthermore, by restricting the relative slip velocity to lie in the same direction as the motive stress, a nondegenerate description under shape perturbation is achieved.

The hydrodynamics of a system of such swimmers requires solving the incompressible Stokes equations with mixed-type boundary conditions. We develop a numerical approach based upon the classical boundary integral formulation for the Stokes equations which consists of a combination of single-layer and double-layer potentials. We apply this model to spherical and ellipsoidal bodies. We discretize the integral equations using a Nystrom method, which leads to a linear system of equations for surface stresses and slip-velocities. The GMRES Krylov subspace method is used to solve the consequent linear system, and the second-order Adams–Bashforth method is used to integrate the bodies' positions and orientations.

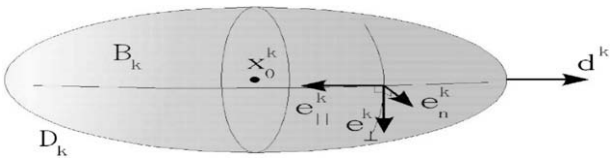

Fig. 1. Surface $\mathbf{D}_k$ corresponding to body $\mathbf{B}_k$.

In Section 2, we discuss boundary conditions and constraints. In Section 3, we describe the boundary integral formulation which we use to compute the dynamics of the locomotors. The numerical scheme used to discretize the boundary integral method and thus approximate the dynamics of the bodies is discussed in Section 4, followed by numerical tests in Section 5 and concluding remarks in Section 6.

2. Fluid dynamical model

We first introduce basic nomenclature. Let $\mathbf{D} = \bigcup_{p=1}^{K} \mathbf{D}_k$ be a closed, multiply-connected surface which is composed of K simply-connected surfaces $\mathbf{D}_k$ (see Fig. 1). We refer to $\mathbf{B}_k$ as the kth body with surface $\mathbf{D}_k$. The following variables are defined for the kth body: $\mathbf{u}^k$ is the surface fluid velocity, p^k is the surface pressure, $\mathbf{f}^k$ is the surface stress exerted on the fluid by surface $\mathbf{D}_k$, $\mathbf{U}_0^k$ is the velocity of the body's centroid $\mathbf{x}_0^k$, $\boldsymbol{\omega}^k$ is an angular velocity of the body, $\mathbf{F}^k$ is the total body force, $\mathbf{T}^k$ is the total body torque, $\mathbf{d}^k$ is the body's orientation vector and is fixed in the body frame, $\mathbf{e}_n^k$ is the outward normal unit vector, $\mathbf{e}_\parallel^k$ is the specified motive stress direction unit vector, and $\mathbf{e}_\perp^k = \mathbf{e}_n^k \times \mathbf{e}_\parallel^k$. Fig. 1 shows the coordinate system formed by the vectors $\mathbf{e}_\parallel^k$, $\mathbf{e}_\perp^k$, and $\mathbf{e}_n^k$ at a point on surface $\mathbf{D}_k$.

The velocity $\mathbf{u}$ and pressure p satisfy Eq. (1) in the exterior of $\mathbf{D}_k$. Our model assumes that in order to propel itself a locomotor exerts a specified surface shear stress (motive stress) on the surrounding fluid given by $\mathbf{f}_\parallel^k = f_\parallel^k \mathbf{e}_\parallel^k$. The prescribed shear stress boundary condition above, which generalizes the constant stress assumption used in [25], in principle takes into account the beating pattern and frequency of the swimmers' flagella (or the detailed chemical kinetics in the case of [17]).

We project the stress $\mathbf{f}^k$ onto $\mathbf{e}_\parallel^k$, $\mathbf{e}_\perp^k$, and $\mathbf{e}_n^k$ as

$$\mathbf{f}^k = \mathbf{e}_n^k \mathbf{e}_n^k \mathbf{f}^k + (\mathbf{I} - \mathbf{e}_n^k \mathbf{e}_n^k)(\mathbf{I} - \mathbf{e}_\perp^k \mathbf{e}_\perp^k)\mathbf{f}^k + (\mathbf{I} - \mathbf{e}_n^k \mathbf{e}_n^k)\left(\mathbf{I} - \mathbf{e}_\parallel^k \mathbf{e}_\parallel^k\right)\mathbf{f}^k = \mathbf{f}_n^k + \left(\mathbf{f}_\parallel^k + \mathbf{f}_\perp^k\right),$$

where $\mathbf{f}_n^k = f_n^k \mathbf{e}_n^k$ and $\mathbf{f}_\perp^k = f_\perp^k \mathbf{e}_\perp^k$. Thus, the unknowns are the normal surface stress amplitude f_n^k, which is strongly dependent on the body's geometry, and the tangential surface stress amplitude $f_\perp^k$, which is generated by the body's rotations.

On the kth body, the surface fluid velocity is of the form

$$\mathbf{u}^k(\mathbf{x}) = \left[\mathbf{U}_0^k + (\boldsymbol{\omega}^k \times (\mathbf{x} - \mathbf{x}_0^k))\right] + \mathbf{u}_{sl}^k, \quad \mathbf{x} \in \mathbf{D}_k.$$

The first term (in brackets) is that associated with solid body translation and rotation. The second, $\mathbf{u}_{sl}^k$, is a slip velocity which we shall assume lies only in the direction of $\mathbf{e}_\parallel^k$, and is also an unknown. The form of $\mathbf{u}^k$ implies a non-penetration condition at the surface $\mathbf{D}_k$. In addition to solving for fluid surface stresses and slip velocities, we must also solve for the centroid velocity $\mathbf{U}_0^k$ and the angular velocity $\boldsymbol{\omega}^k$ for each body. Also, the flow at infinity is assumed to be quiescent. In summary, the boundary conditions are

$$(\mathbf{I} - \mathbf{e}_n^k \mathbf{e}_n^k)(\mathbf{I} - \mathbf{e}_\perp^k \mathbf{e}_\perp^k)\mathbf{f}^k = f_\parallel^k \mathbf{e}_\parallel^k = \mathbf{f}_\parallel^k, \tag{2}$$

$$\mathbf{u}_{sl}^k \cdot \mathbf{e}_n^k = 0, \quad \mathbf{u}_{sl}^k \cdot \mathbf{e}_\perp^k = 0, \quad \mathbf{u}|_\infty = 0. \tag{3}$$

We close the system by requiring the net force and net torque for the kth body to be equivalent to zero:

$$\mathbf{F}^k = 0, \quad \mathbf{T}^k = 0. \tag{4}$$

Without going into specific details, we did investigate other models for simulating interactions of active locomotors. However, these models, which only solved for one of the three surface traction components while specifying the other two, had degeneracies in the limit of aspect ratio (ratio of semi-major axis length to semi-minor axis length) approaching one and thus led to systems that were singular. We subsequently found that solving for two of the three surface traction components results in nonsingular systems in this limit, and also results in spherical bodies that do rotate due to hydrodynamic interactions.

3. Boundary integral formulation

We represent solutions to the Stokes equations in terms of a boundary integral formulation. Our formulation for Eqs. (1)–(4) is based on a combination of fundamental solutions (free-space Green's functions of Stokes flow) to the Stokes equations, the Stokeslet ($\mathbf{G}$) and the stresslet ($\mathbf{T}$)

$$\mathbf{g}_{ij}(\mathbf{x},\mathbf{y}) = \frac{\delta_{ij}}{R} + \frac{R_i R_j}{R^3}, \tag{5}$$

$$\mathbf{t}_{ijk}(\mathbf{x},\mathbf{y}) = -6\frac{R_i R_j R_k}{R^5}, \tag{6}$$

$$\mathbf{R} = \mathbf{x} - \mathbf{y}, \quad R = |\mathbf{R}|, \tag{7}$$

and involves boundary values of velocity and stress. It is a mixed formulation since it is based on the combination of the single and double layer potentials. The nondimensionalized formulation for $\mathbf{y} \in \mathbf{D}_k$ is

$$u_l^k(\mathbf{y}) = -\frac{1}{4\pi\mu}\int_{\cup \mathbf{D}_k} \mathbf{f}_i^k(\mathbf{x})\mathbf{g}_{il}(\mathbf{x},\mathbf{y})dS_x \tag{8}$$

$$+\frac{1}{4\pi}\int_{\cup \mathbf{D}_k}^{PV} u_i^k(\mathbf{x})\mathbf{t}_{ijl}(\mathbf{x},\mathbf{y})\mathbf{e}_{n_j}^k(\mathbf{x})dS_x, \tag{9}$$

$$\mathbf{u}_{sl}^k(\mathbf{y})\cdot\mathbf{e}_n^k(\mathbf{y}) = 0, \quad \mathbf{u}_{sl}^k(\mathbf{y})\cdot\mathbf{e}_\perp^k(\mathbf{y}) = 0, \tag{10}$$

$$\mathbf{F}^k = \int_{\mathbf{D}_k} \mathbf{f}^k dS_x = 0, \tag{11}$$

$$\mathbf{T}^k = \int_{\mathbf{D}_k} (\mathbf{r}^k \times \mathbf{f}^k) dS_x = 0. \tag{12}$$

Eqs. (8)–(12) are nondimensionalized using the semi-major axis length c of the ellipsoidal swimmer (radius a for a spherical swimmer), the characteristic magnitude of the flow velocity $U \sim \bar{f}c/\mu$, where $\bar{f}$ is the average value of $f_\parallel$, and the fluid viscosity μ. The boundary conditions are that the shear stress component $\mathbf{f}_\parallel^k$ is specified, and that the only nonzero slip velocity component is $\mathbf{u}_{sl}^k \cdot \mathbf{e}_\parallel^k$ at each interface $\mathbf{D}_k$. We complete the formulation by requiring the net body force and torque to be equal to zero for each surface $\mathbf{D}_k$.

4. Numerical method

Throughout this paper we focus on the dynamics of spherical and ellipsoidal bodies. The spheres have fixed radius $a = 1.0$, while the prolate ellipsoids have fixed semi-major axis length $c = 1.0$ (major axis length is $2c = 2.0$) and semi-minor axis length b. The aspect ratio is $\mathrm{AR} = c/b$.

We discretize the integral equation system above using the Nystrom collocation method. The surface of the sphere or ellipsoid is discretized using a uniformly-spaced $\theta - \phi$ mesh($\theta \in [0,\pi]$ is polar angle, $\phi \in [0,2\pi]$ is azimuthal angle in spherical coordinates): $\theta_j = \pi j/(N_1 - 1),\ j = 0,1,\ldots,N_1 - 1$, and $\phi_j = 2\pi j/(N_2 - 1),\ j = 0,1,\ldots,N_2 - 1$, where N_1 and N_2 are integers. The Cartesian coordinates of a point on a sphere (centered at origin) corresponding to a $\theta - \phi$ pair are $(x,y,z) = (\sin\theta\cos\phi, \sin\theta\sin\phi, \cos\theta)$, while the Cartesian coordinates of a point on an ellipsoid (centered at origin) corresponding to a θ–ϕ pair are $(x,y,z) = (\sqrt{\Gamma^2 - 1}\sin\theta\cos\phi, \sqrt{\Gamma^2 - 1}\sin\theta\sin\phi, \Gamma\cos\theta)\sqrt{c^2 - a^2}$, where the ratio of major axis length to distance between the foci is $\Gamma = c/\sqrt{c^2 - a^2}$.

The trapezoidal rule on the surface is carried out as the tensor product of one-dimensional trapezoidal rules

$$\int_0^{2\pi}\int_0^{\pi} f(\theta,\phi)d\theta d\phi \approx h_\theta h_\phi \sum_{k=0}^{N_2-1}\sum_{j=0}^{N_1-1} w_j w_k f(\theta_j,\phi_k), \tag{13}$$

where $w_j = 1,\ j = 1,2,\ldots,N_1 - 2,\ w_k = 1, k = 1,2,\ldots,N_2 - 2,\ w_j = 1/2,\ j = 0, N_1 - 1,\ w_k = 1/2,\ k = 0, N_2 - 1,\ h_\theta = \pi/N_1$ and $h_\phi = 2\pi/N_2$. This is slightly modified in our implementation since we use only one point to discretize each pole, giving the total number of points $N = (N_1 - 2)(N_2 - 1) + 2$.

It is important to note that the single-layer and the double-layer integrals have singularities whenever $\mathbf{x} = \mathbf{y}$ that if left untreated will affect the order of accuracy in the trapezoidal quadrature. For the single-layer term, we apply a subtraction technique,

$$\int_D \mathbf{f}_i(\mathbf{x})\mathbf{G}_{ik}(\mathbf{x},\mathbf{y})dS_x = \int_D [\mathbf{f}_i(\mathbf{x}) - \mathbf{f}_i(\mathbf{y})]\mathbf{G}_{ik}(\mathbf{x},\mathbf{y})dS_x + \mathbf{f}_i(\mathbf{y})\int_D \mathbf{G}_{ik}(\mathbf{x},\mathbf{y})dS_x, \tag{14}$$

thus reducing the order of the singularity in the first term on the right hand side of Eq. (14), which may now be evaluated with the trapezoidal rule to second-order accuracy. We evaluate $\int_D \mathbf{G}_{ik}(\mathbf{x},\mathbf{y})dS_x$ (second term in Eq. (14)) using a quadrature method based on a transformation technique due to Sidi [26]. Similarly, for the double-layer term, we apply a similar technique:

$$\int_D u_i(\mathbf{x})\mathbf{T}_{ijk}(\mathbf{x},\mathbf{y})n_j(\mathbf{x})dS_x = \int_D [u_i(\mathbf{x}) - u_i(\mathbf{y})]\mathbf{T}_{ijk}(\mathbf{x},\mathbf{y})n_j(\mathbf{x})dS_x - 4\pi u_k(\mathbf{y}), \tag{15}$$

which uses a well-known identity [19], and again reduces the order of the singularity in the first term on the right hand side of Eq. (15). The trapezoidal rule will now yield second-order accuracy. For each body $\mathbf{D}_k$, there are five equations per point for

N points, as well as six additional equations generated by the requirement that the net force must be zero and the net torque must also be zero. Thus, the size of the linear system is $((5N+6)p)^2$. The resulting linear system

$$\mathbf{Aq} = \mathbf{b} \tag{16}$$

is solved for $\mathbf{q}$ using GMRES [21]. The success of an iterative linear solver largely depends on an effective preconditioner, which may result in significant speed-ups. We apply right preconditioning, which leaves the right-hand side of Eq. (16) unchanged

$$(\mathbf{AP}^{-1})(\mathbf{Pq}) = \mathbf{b}, \tag{17}$$

where $\mathbf{P}$ represents the preconditioning matrix (an approximation to $\mathbf{A}$). Solving the preconditioned system above involves two main steps. First, we define $\mathbf{z} = \mathbf{Pq}$ and solve $\mathbf{AP}^{-1}\mathbf{z} = \mathbf{b}$ for $\mathbf{z}$ using GMRES. Note that $\mathbf{P}^{-1}$ is never actually computed, but the action of $\mathbf{P}^{-1}$ on $\mathbf{z}$ is computed. Second, we solve $\mathbf{Pq} = \mathbf{z}$ for $\mathbf{q}$ using a fast sparse direct solver. The preconditioning matrix $\mathbf{P}$, a very sparse approximation to $\mathbf{A}$, is the main block diagonal of $\mathbf{A}$ (nonoverlapping blocks are 5×5 matrices) and the last $6p$ rows and columns of $\mathbf{A}$, where p is the number of bodies. We apply extrapolation in conjunction with preconditioning in order to reduce the number of iterations even further by improving the initial guess vectors that are needed to start each GMRES cycle (i.e., use solutions from the two previous time levels to extrapolate initial guess). Table 3 lists the average number of GMRES iterations for some of the two-body interaction tests discussed in Section 5.

Each body's position and orientation are updated by integrating the ordinary differential equations

$$\frac{d}{dt}\mathbf{x}_0^k = \mathbf{U}_0^k, \quad \frac{d}{dt}\mathbf{d}^k = \boldsymbol{\omega}^k \times \mathbf{d}^k, \tag{18}$$

for $\mathbf{x}_0^k$ and $\mathbf{d}^k$ using the second-order Adams–Bashforth multistep scheme.

5. Numerical tests

For all the numerical tests that follow we take $\mathbf{f}_{\|} = f_{\|}\hat{\boldsymbol{\theta}}$, where $\hat{\boldsymbol{\theta}}$ is the polar unit vector directed along the lines of longitude (see Appendix A). Note too that the orientation vector $\mathbf{d}^k$ of each swimmer is along the polar axis and for the stress distributions used here is also the direction of swimming for single bodies.

5.1. One sphere

We test the numerical method presented in Section 4 for the case of a single spherical swimmer by comparing the numerical results for the normal stress, normal velocity, and tangential velocity distributions to the analytical solution derived in Appendix A. For $f_{\|} = -\sin\theta$, the normal and tangential ($\hat{\boldsymbol{\theta}}$-direction) velocities are $u = (\cos\theta/3)r^{-3}$ and $v = (\sin\theta/6)r^{-3}$. Note that for this particular case, the velocity field decays rapidly as r^{-3} and results in weak interactions among two or more swimmers.

Table 1
Sphere, (a) normal stress errors, (b) normal velocity errors, and (c) tangential velocity errors. $f_{\|} = -\sin\theta$.

N_1	N_2	Error (L_∞)	Error (L_2)	Convergence rate (L_∞)	Convergence rate (L_2)
(a)					
4	128	1.197e+00	9.173e−01		
8	128	1.470e−01	9.596e−02	3.03	3.26
16	128	3.173e−02	1.821e−02	2.21	2.40
32	128	7.717e−03	4.003e−03	2.04	2.19
64	128	1.938e−03	9.359e−04	1.99	2.10
128	128	4.478e−04	2.238e−04	2.11	2.06
(b)					
4	128	5.750e−01	4.546e−01		
8	128	6.979e−02	5.234e−02	3.04	3.12
16	128	1.416e−02	1.032e−02	2.30	2.34
32	128	3.241e−03	2.327e−03	2.13	2.15
64	128	7.776e−04	5.543e−04	2.06	2.07
128	128	1.902e−04	1.351e−04	2.03	2.04
(c)					
4	128	1.179e−01	8.335e−02		
8	128	2.484e−02	1.912e−02	2.25	2.12
16	128	6.125e−03	4.679e−03	2.02	2.03
32	128	1.577e−03	1.171e−03	1.96	2.00
64	128	4.060e−04	2.951e−04	1.96	1.99
128	128	1.044e−04	7.450e−05	1.96	1.99

Table 2
Ellipsoid, (a) normal stress errors, (b) normal velocity errors, and (c) tangential velocity errors. $f_{\|} = -\sin\theta$.

N_1	N_2	Error (L_∞)	Error(L_2)	Convergence rate (L_∞)	Convergence rate (L_2)
(a)					
4	128	2.988e+00	2.216e+00		
8	128	3.024e−01	1.910e−01	3.30	3.54
16	128	6.372e−02	3.539e−02	2.25	2.43
32	128	1.476e−02	7.657e−03	2.11	2.21
64	128	3.406e−03	1.768e−03	2.12	2.12
128	128	7.341e−04	4.151e−04	2.21	2.09
(b)					
4	128	1.494e+00	1.136e+00		
8	128	1.576e−01	1.113e−01	3.24	3.35
16	128	3.187e−02	2.168e−02	2.31	2.36
32	128	7.287e−03	4.861e−03	2.13	2.16
64	128	1.748e−03	1.154e−03	2.06	2.07
128	128	4.287e−04	2.818e−04	2.03	2.03
(c)					
4	128	1.565e−01	1.107e−01		
8	128	4.435e−02	3.067e−02	1.82	1.85
16	128	1.197e−02	7.835e−03	1.89	1.97
32	128	3.105e−03	2.001e−03	1.95	1.97
64	128	8.234e−04	5.096e−04	1.92	1.97
128	128	2.134e−04	1.293e−04	1.95	1.98

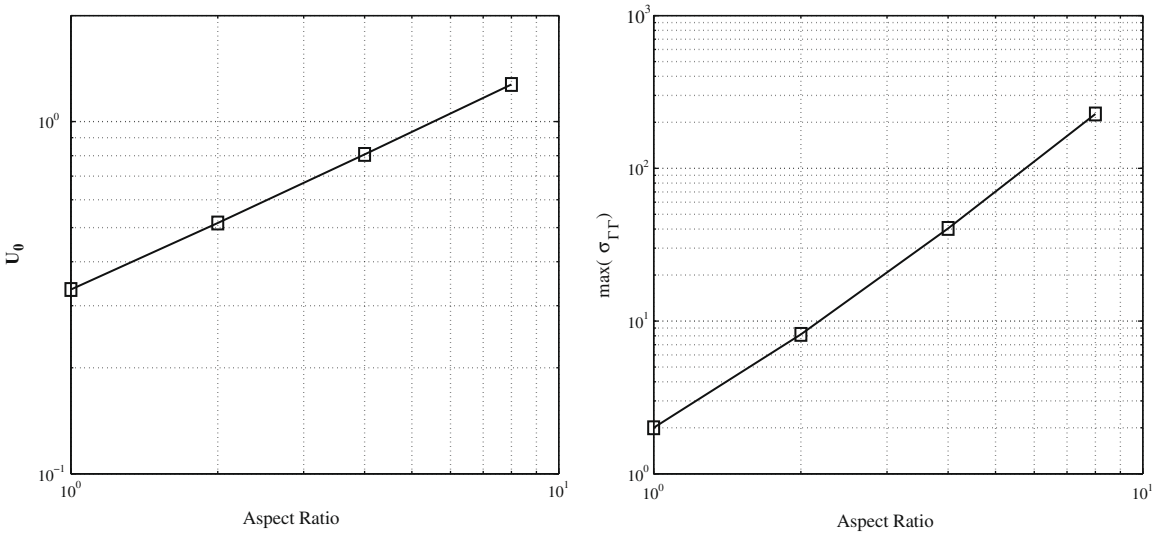

(a) Centroid velocity $\mathbf{U}_0$ versus aspect ratio. (b) Maximum normal stress versus aspect ratio.

Fig. 2. Centroid velocity and maximum normal stress versus aspect ratio for a single ellipsoidal locomotor. $f_{\|} = -\sin\theta$.

We compute the errors in the L_∞ and the L_2 norms, which are summarized in Table 1. The grid used is uniform in the polar (θ) and azimuthal directions (ϕ). We set $N_2 = 128$ constant (number of points in the ϕ direction), and increase N_1 (number of points in the θ direction) from 4 to 128. For all results shown, the GMRES tolerance is 10^{-8}.

We can clearly see that the convergence rate in N_1 is of design order accuracy for the trapezoidal rule, i.e. the numerical spatial discretization is second-order accurate with respect to N_1. We do not show the more rapid convergence rates with respect to N_2, since the functions in this test problem are periodic in ϕ. Note that applying the trapezoidal rule to smooth periodic functions results in superalgebraic convergence.

5.2. One ellipsoid

Next, we test the numerical method presented in Section 4 for the case of a single prolate ellipsoidal swimmer by comparing the numerical results for the normal stress, normal velocity, and tangential velocity distributions to the analytical

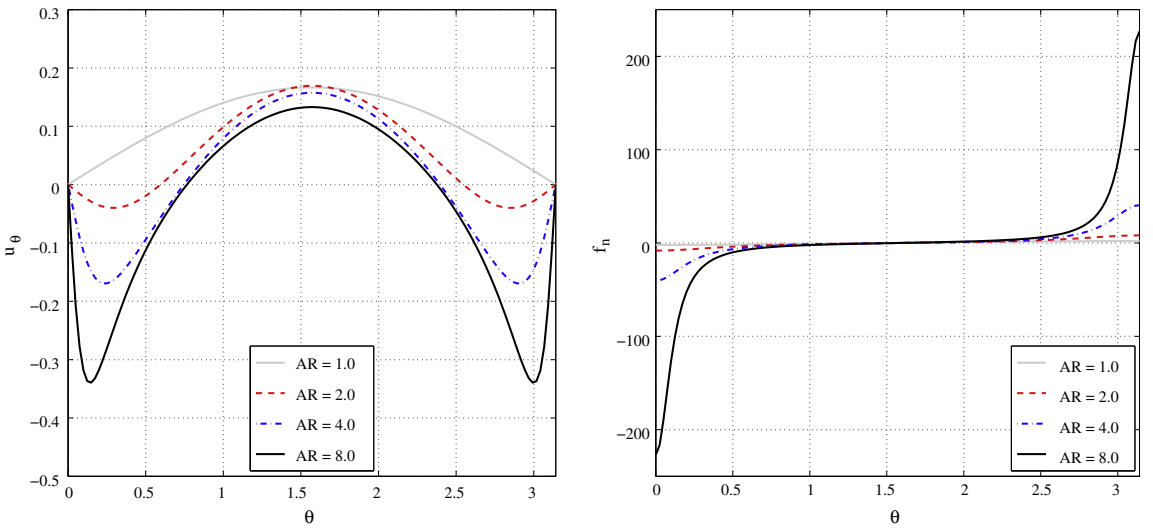

(a) Tangential velocity profiles. (b) Normal stress profiles.

Fig. 3. Tangential velocity and normal stress profiles for ellipsoidal locomotor. $f_\parallel = -\sin\theta$.

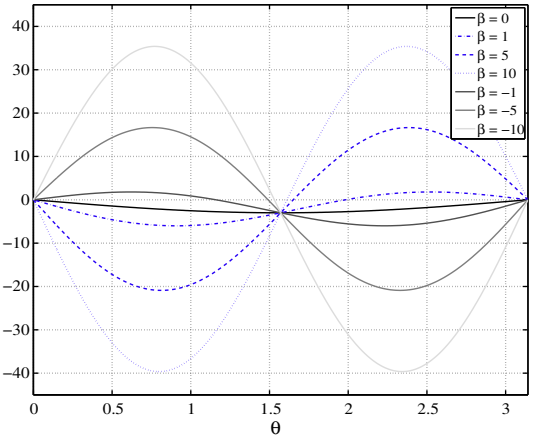

Fig. 4. Tangential stress distribution functions based on [13]. $f_\parallel = -3\sin\theta - \frac{15}{2}\beta\sin\theta\cos\theta$. The dotted curves are for $\beta > 0$ (*pullers*), the gray curves are for $\beta < 0$ (*pushers*), while the black curve is for $\beta = 0$.

solution derived in Appendix B. We compute the errors in the L_∞ and L_2 norms, which are summarized in Table 2 for an ellipsoid with aspect ratio AR $= 1.34$ and $\Gamma = 1.5$.

The grid used is uniform in the polar and azimuthal directions. We set $N_2 = 128$ (number of points in the ϕ direction), and increase N_1 (number of points in the θ direction) from 4 to 128. For all results shown, the tangential stress distribution function is $f_\parallel = -\sin\theta$, and the GMRES tolerance is 10^{-8}.

Again, we can clearly see that the convergence rate in N_1 is second-order accurate with respect to N_1. We do not show the convergence rates with respect to increasing N_2, but note that they are typically higher than the case shown due to the periodicity in the ϕ direction.

In Fig. 2(a) and (b), we plot the centroid velocity U_0 and the maximum normal stress versus aspect ratio AR for a single ellipsoidal locomotor. Here, $c = 2$ and $a = b = 2/\text{AR}$. The tangential stress distribution is $f_\parallel = -\sin\theta$. We find that both U_0 and the maximum normal stress grow linearly with the aspect ratio (at least over this range). Finally, we plot the tangential velocity and normal stress profiles for ellipsoids with AR ranging from 1.0 to 8.0 in Fig. 3(a) and (b), respectively.

5.3. Two interacting bodies

In this section, we discuss several simulations for two interacting spheres and ellipsoids.

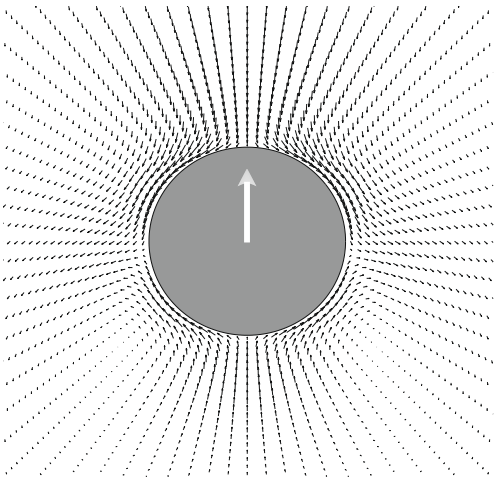

Fig. 5. Flow velocity field (in reference frame of locomotor) for a *puller* ($\beta = 10$). The normal and tangential ($\hat{\boldsymbol{\theta}}$-direction) velocities are $u = \cos\theta(r^{-3} - 1) + (3\beta/4)(3\cos^2\theta - 1)(r^{-4} - r^{-2})$ and $v = \sin\theta(r^{-3}/2 + 1) + (3\beta/2)\sin\theta\cos\theta r^{-4}$.

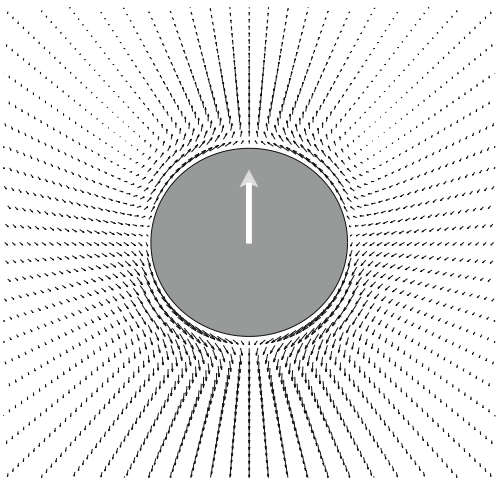

Fig. 6. Flow velocity field (in reference frame of locomotor) for a *pusher* ($\beta = -10$). The normal and tangential ($\hat{\boldsymbol{\theta}}$-direction) velocities are $u = \cos\theta(r^{-3} - 1) + (3\beta/4)(3\cos^2\theta - 1)(r^{-4} - r^{-2})$ and $v = \sin\theta(r^{-3}/2 + 1) + (3\beta/2)\sin\theta\cos\theta r^{-4}$.

All of the two-sphere tests were run with $\Delta t = 2.5 \times 10^{-2}$, GMRES tolerance equal to 10^{-6}, $N_1 = 48$ and $N_2 = 24$. The two-ellipsoid tests had the same parameters except that the time step $\Delta t = 1.5 \times 10^{-2}$ for AR = 2.0 and $\Delta t = 5.0 \times 10^{-3}$ for AR = 8.0.

The first two-sphere interaction test has the following initial conditions: the orientation vectors of the two swimmers are initially anti-aligned (this defines $\alpha_0 = \pi$, for which $\mathbf{d}^1 \cdot \mathbf{d}^2 = \cos\alpha_0$ initially), and they are swimming towards one another with an offset (see Fig. 7(a)). The initial center-to-center δ_y separation distances vary from 2.5 to 10.0, while initial center-to-center δ_z separation distances are 10.0. The invariant tangential stress distribution we apply for all interaction tests yields the slip velocity distribution used in [13] for a single swimmer, and is given by $f_{\|} = -3\sin\theta - \frac{15}{2}\beta\sin\theta\cos\theta$, which is plotted for various positive and negative values of β in Fig. 4. Note that the β-term in the stress distribution above does not contribute to the mean stress, whereas the first term does. Locomotors with this stress distribution are referred to as *pullers* for $\beta > 0$, since most of the shear stress actuation occurs in the anterior region, and as *pushers* for $\beta < 0$. The velocity field generated by a single *puller* with $\beta = 10$ is shown in Fig. 5 (in reference frame of locomotor), while the velocity field generated by a single *pusher* with $\beta = -10$ is shown in Fig. 6 (in reference frame of locomotor). Note that the centroid velocity $U_0 = 1.0$ for a single spherical *puller* or *pusher*.

For all interaction tests we find that $\beta = 0$, which is a symmetric shear stress distribution, results in velocity fields that decay as r^{-3} and therefore yields very weak interactions between two swimmers, while distributions with $\beta \neq 0$ break the symmetry, resulting in velocity fields that decay as r^{-2} and thus stronger and more interesting interactions. For this reason the value of β is typically chosen to be 10 (higher values of β result in stronger interactions).

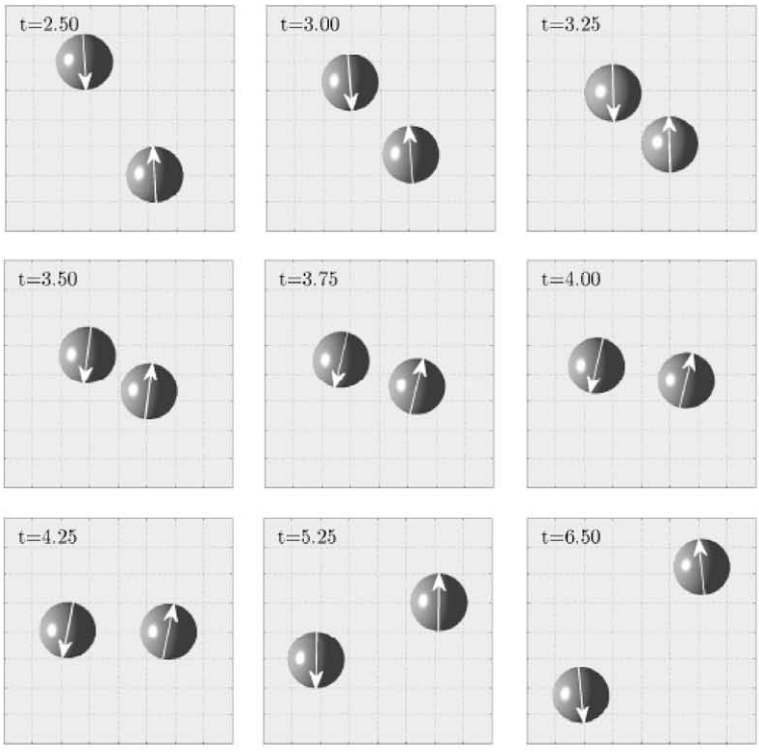

(a) $\beta = 10$, $\delta_y = 3.0$ and $\delta_z = 10.0$.

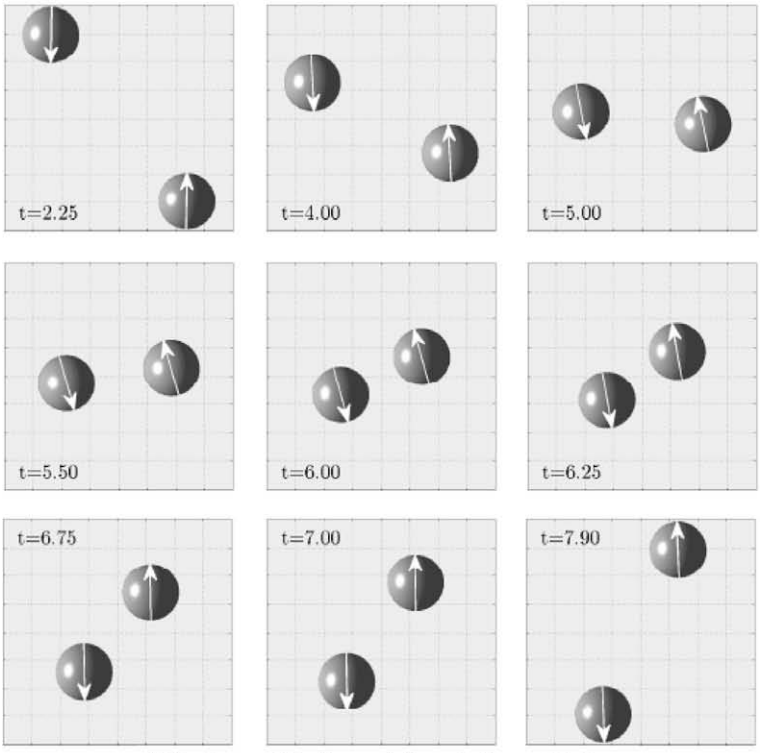

(b) $\beta = -10$, $\delta_y = 4.5$ and $\delta_z = 10.0$.

Fig. 7. Interaction history of two spherical swimmers ((a) *pullers*, (b) *pushers*) with initial condition $\alpha_0 = \pi$, and $\Delta t = 2.5 \times 10^{-2}$. The horizontal and vertical axes in each subplot depict the y and z directions.

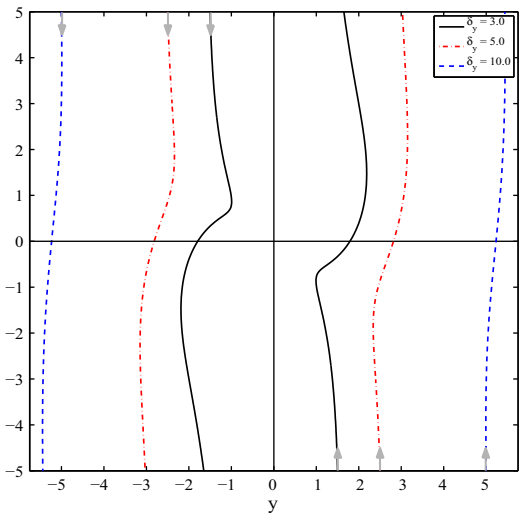

(a) $\delta_y = 3.0$ (solid line), 5.0 (dash-dotted line), 10.0 (dashed line), $\beta = 10$.

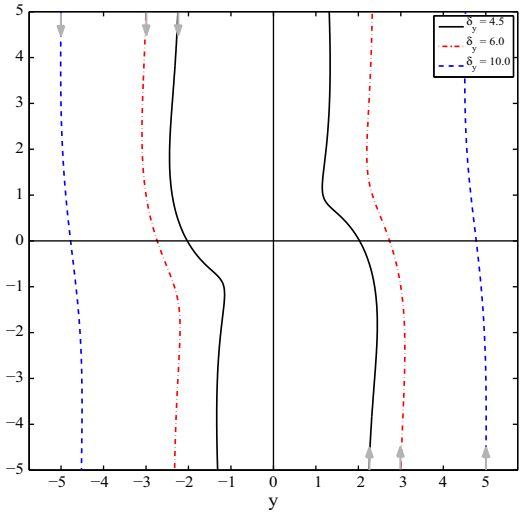

(b) $\delta_y = 4.5$ (solid line), 6.0 (dash-dotted line), 10.0 (dashed line), $\beta = -10$.

Fig. 8. Trajectories of two spherical swimmers ((a) *pullers*, (b) *pushers*) with initial condition $\alpha_0 = \pi$.

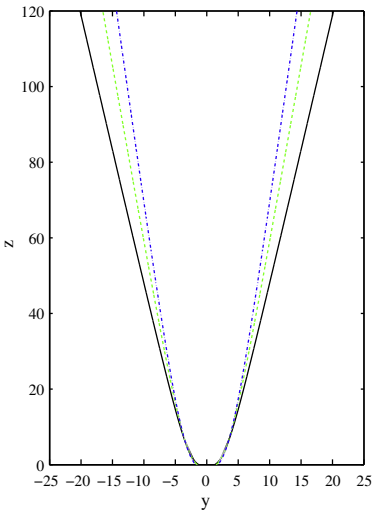

(a) $\beta = 10$, and initial conditions $\delta_y = 2.5$ (solid line), 3.0 (dashed line), 3.5 (dash-dotted line).

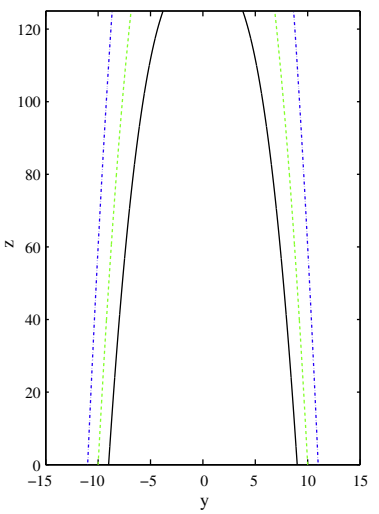

(b) $\beta = -10$, and initial conditions $\delta_y = 18.0$ (solid line), 20.0 (dashed line), 22.0 (dash-dotted line).

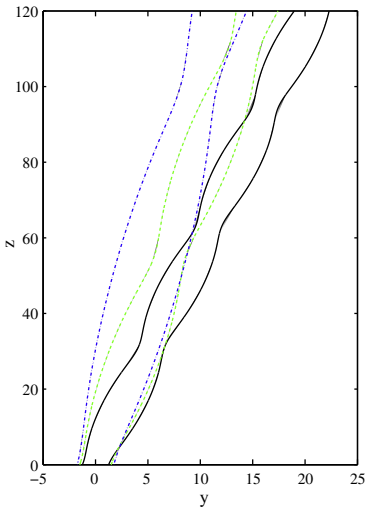

(c) $\beta = 2$ for left sphere, while $\beta = -2$ for right sphere. Initial conditions are $\delta_y = 2.5$ (solid line), 3.0 (dashed line), 3.5 (dash-dotted line).

Fig. 9. Trajectories of two spherical swimmers ((a) *pullers*, (b) *pushers*, (c) *puller* and *pusher*) with initial condition $\alpha_0 = 0$.

First, we will describe the interaction of the two spherical *pullers* for $\beta = 10$, $\delta_y = 3.0$ and $\delta_z = 10.0$. We will then summarize results from a very similar two-sphere test found in Ishikawa et al. [13] (refer to pp. 148–149 and Figs. 18(a)–(h) and 19) with initial conditions: $\alpha_0 = \pi$, $\beta = 5$, $\delta_y = 1$, and $\delta_z = 10$. Although the initial conditions for both tests are not exactly the same, it is still possible to compare the qualitative behavior of the locomotor interactions for the case of two *pullers* swimming towards one another ($\alpha_0 = \pi$).

Fig. 7 shows the interaction of these two spherical *pullers*. Their direction vectors, $\mathbf{d}^1$ and $\mathbf{d}^2$, are also shown to reveal changes in orientation. The spheres initially move towards one another, while rotating counter-clockwise (Fig. 7(a.1)–(a.3)). Upon close interaction, they reverse the rotation direction, rotate clockwise and push apart (Fig. 7(a.4)–(a.7)). Finally,

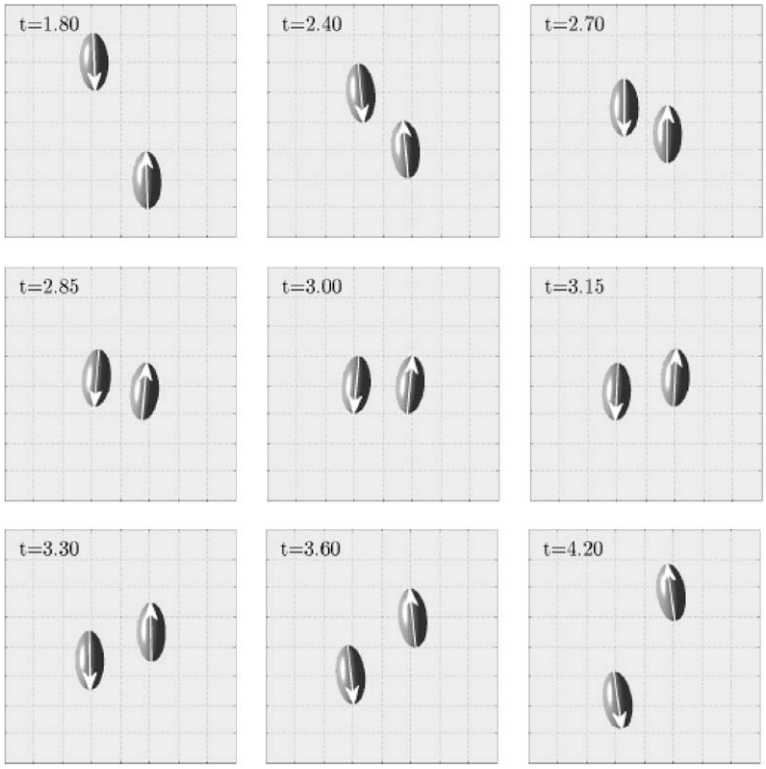

Fig. 10. Interaction history of two ellipsoidal swimmers (*pullers*, AR = 2.0) with $\beta = 10$, and initial conditions $\alpha_0 = \pi$, $\delta_y = 2.0$ and $\delta_z = 10.0$. $\Delta t = 1.5 \times 10^{-2}$. The horizontal and vertical axes in each subplot depict the y and z directions. $N_1 = 48$ and $N_2 = 24$.

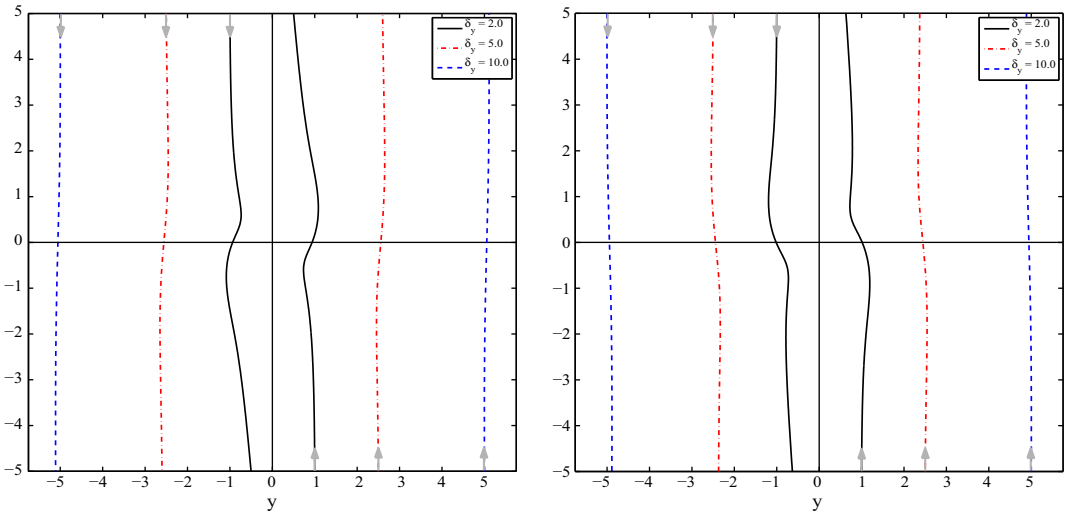

Fig. 11. Trajectories of two ellipsoidal swimmers ((a) *pullers*, (b) *pushers*) (AR = 2.0) with initial conditions $\alpha_0 = \pi$, and $\delta_y = 2.0$ (solid line), 5.0 (dash-dotted line), 10.0 (dashed line).

as the locomotors swim apart, they change the direction of their rotation once more to counter-clockwise (Fig. 7(a.8)–(a.9)). The centroid trajectories of two spherical locomotors for various values of δ_y are plotted in Fig. 8(a) for $\beta = 10$.

There are important differences with the results of [13]. There the spheres initially move towards one another, while rotating in the clockwise direction (Fig. 18(a)–(c) of [13]). In the near field, they continue rotating in the clockwise direction

and push apart (Fig. 18(d)–(f) of [13]). Finally, as the locomotors move apart, they change the direction of their rotation to the counter-clockwise direction (Fig. 18(g)–(h) of [13]). Hence, the main difference between our results and those of [13] for this particular test is that the locomotors in our model show a more complex rotational dynamics. As a result, the final positions and orientations vary significantly from those of [13].

In the second test, we increase the offset ($\delta_y = 4.5$) and change the swimmer type to *pushers* with $\beta = -10$. The interactions in this case are shown in Fig. 7(b.1)–(b.9). The spheres initially push away from one another in the y-direction and move toward one another in the z-direction while rotating clockwise (Fig. 7(b.1)). They later swim toward one another and rotate counter-clockwise (Fig. 7(b.2)–(b.6)), and move away from each other while rotating clockwise as they swim apart (Fig. 7(b.7)–(b.9)). The centroid trajectories are plotted in Fig. 8(b).

Next, we discuss three tests for two interacting spheres which swim side by side and are initially oriented in the same direction ($\alpha_0 = 0$). For these three cases, (a) both are *pullers* with $\beta = 10$, (b) both are *pushers* with $\beta = -10$, and (c) one is a *puller* ($\beta = 10$) and the other a *pusher* ($\beta = -10$). In the first case (a), the spheres push each other away in the y-direction and rotate away from each other (sphere on the right rotates clockwise, while sphere to the left rotates counter-clockwise), while in the second case (b) they pull each other towards one another and rotate towards one another. For case (c), the spheres' swimming motions are oscillatory, whereby they swim away from and then toward one another. Long-time simulations were necessary to see these motions, which are similar in nature to those recently observed by Pooley et al. in [18], whose work investigated the effect of swimming stroke phase on interactions between two model swimmers. The centroid trajectories for all three cases are plotted in Fig. 9(a)–(c).

We now discuss simulations for two interacting ellipsoids with AR = 2.0 and AR = 8.0. The first set of simulations have the following initial conditions for both aspect ratios: $\alpha_0 = \pi$, initial separation distances δ_y vary from 2.0 to 10.0, while initial separation distances $\delta_z = 10.0$, and $\beta = 10$ and -10, respectively.

Fig. 10 shows the interaction history of two ellipsoidal swimmers with AR = 2.0 for $\beta = 10$, $\delta_y = 2.0$ and $\delta_z = 10.0$. As for the first two-sphere test, the ellipsoids initially move toward one another and rotate counter-clockwise toward one another (Fig. 10(a)–(b)), then push away and rotate (clockwise) away from each other (Fig. 10(c)–(e)), and finally change the direction of their rotation once more (to counter-clockwise) as they swim apart (Fig. 10(f)–(i)). The centroid trajectories for the ellipsoidal tests for various values of δ_y are plotted in Fig. 11(a)–(b) (AR = 2.0) for $\beta = 10$.

Centroid trajectories for two interacting ellipsoids with higher aspect ratio (AR = 8.0) are plotted in Fig. 12(a)–(b) for $\beta = 10$, $\delta_z = 10.0$, and various values of δ_y. The translational and rotational dynamics are qualitatively similar to the AR = 2.0 ellipsoid tests described above, but the interactions are notably weaker.

We repeat and discuss only these particular two-sphere tests for two ellipsoids (similar initial parameters and stress distributions), since we find that tests performed for two spheres or ellipsoids with similar parameters, initial conditions, and surface stress distributions $f_{\|}$ result in qualitatively similar behavior.

The final two-ellipsoid interaction test has the following initial conditions: $\alpha_0 = \pi/2$, initial separation distance $\delta_y = 2.75$, while initial separation distance $\delta_z = 8.0$, and $\beta = 10$. Fig. 13(a)–(f) show the interactions for this simulation, which result in significant changes in the initial orientations of both swimmers. The swimmer which initially swims in the positive z-direction rotates clockwise, while the second swimmer rotates counter-clockwise.

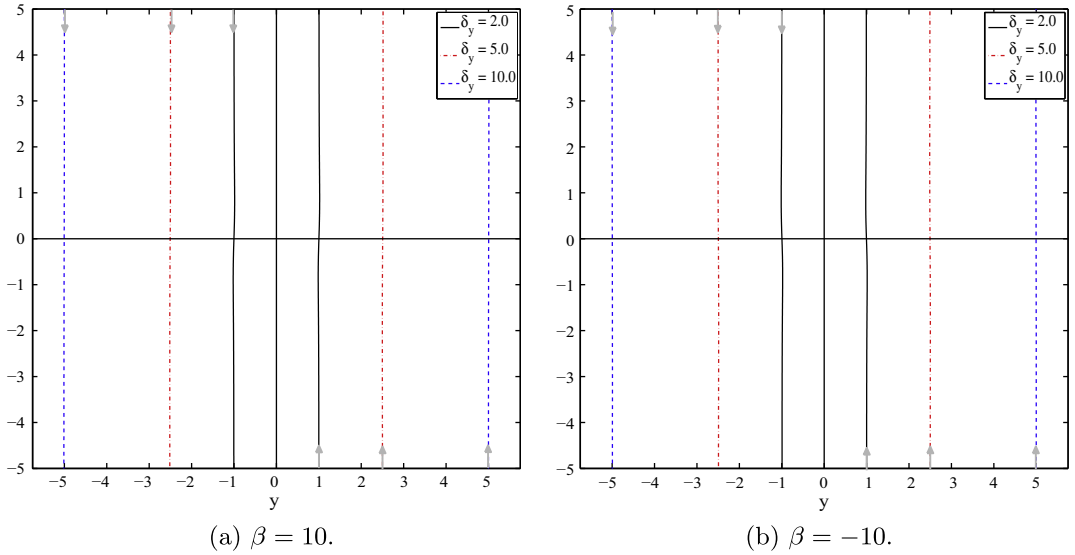

Fig. 12. Trajectories of two ellipsoidal swimmers ((a) *pullers*, (b) *pushers*) (AR = 8.0) with initial conditions $\alpha_0 = \pi$, and $\delta_y = 2.0$ (solid line), 5.0 (dash-dotted line), 10.0 (dashed line).

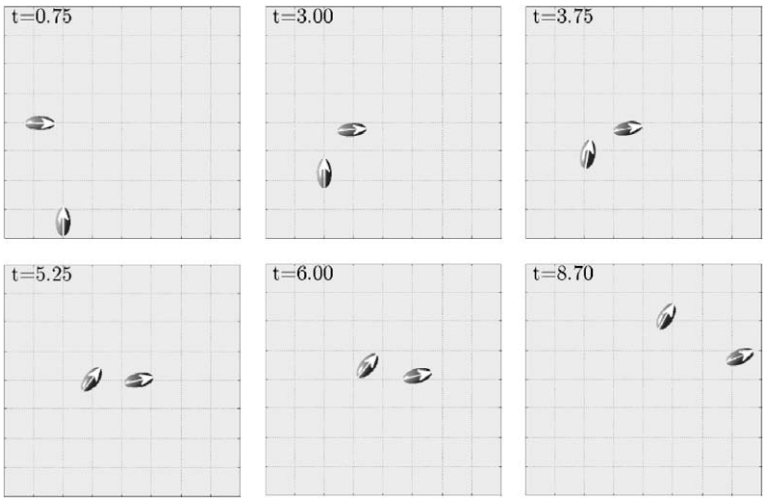

Fig. 13. Interaction history of two ellipsoidal *pullers* (AR = 2.0) with $\beta = 10$, and initial conditions $\alpha_0 = \pi/2,\ \delta_y = 2.75$ and $\delta_z = 8.0$. $\Delta t = 1.5 \times 10^{-2}$. The horizontal and vertical axes in each subplot depict the y and z directions. $N_1 = 48$ and $N_2 = 24$.

Table 3
Average number of GMRES iterations in one time step. $\beta = 10$.

AR	α_0	δ_y	δ_z	GMRES iter.[a]	GMRES iter.[b]
1.0	π	3.00	10.0	64.6	17.4
2.0	π	2.00	10.0	77.5	13.6
2.0	$\pi/2$	2.75	8.0	67.9	9.6

[a] Without preconditioning and extrapolation.
[b] With preconditioning and extrapolation.

In order to give a sense of the computational cost involved in the above simulations, Table 3 lists the average number of iterations per time step for the GMRES solver with and without preconditioning and extrapolation for several of the test cases described above. Results are shown for three of the two sphere and two ellipsoid interaction tests, which resulted in the closest and strongest interactions and thus the largest number of GMRES iterations out of all the tests. Note that preconditioning and extrapolation significantly increases the computational efficiency of the method.

6. Conclusions and discussion

In this paper, we develop and test a mathematical model for simulating the hydrodynamic interactions of multiple spherical or ellipsoidal active swimmers in Stokes flow. The model consists of a mixed boundary-integral formulation with a specified tangential stress boundary condition.

Analytic solutions are derived for a single locomoting sphere and ellipsoid (with prescribed tangential stress distribution) based on spherical and ellipsoidal harmonics, respectively, and are used to demonstrate that the Nystrom spatial discretization is of design order accuracy (second-order). The effects of varying aspect ratio are also investigated for a single prolate ellipsoid, where we find that the magnitudes of the centroid velocity and maximum normal stress are linearly dependent on the aspect ratio, within the range that we investigate.

We simulate the hydrodynamic interactions of two spherical and ellipsoidal swimmers with various stress distributions and initial conditions in an infinite fluid otherwise at rest. Different invariant tangential stress distributions are applied, which are based on the single swimmer surface velocity distributions used in [13], and correspond to *pushers*, for which most of the shear stress actuation occurs in the posterior region, and *pullers*, for which most of the stress actuation occurs in the anterior region. For studies using slender body *pushers* and *pullers* see [23].

Three orientational configurations are tested, namely (a) two swimmers initially facing each other, (b) two swimmers initially oriented at a right angle with respect to one another, and (c) two swimmers initially placed parallel to one another (pairwise swimming). For cases (a) and (b), we find that the body-body interactions are complex and rich, where the orientations and trajectories of each body undergo large, nontrivial changes. For the third case (c), we find three different types of motions, depending on the specified stress distributions. The first two types of interactions for pairwise swimming are (i) repulsive swimming (Fig. 9(a)) and (ii) attractive swimming (Fig. 9(b)), where the two locomotors repel and attract one another, respectively. These motions are unstable, since the two bodies will eventually stop swimming in the same net direction. However, the third type of swimming motion is very interesting and beautiful (see Fig. 9(c)), and occurs when one swimmer is a *pusher*

while the other is a *puller*. These stable oscillatory swimming patterns are highly sensitive to the distance between the centroids of the locomotors. In fact, we find that changes of roughly .5 in the distance between the centroids from centroid distance lead to a doubling (or halving) of the period depending on whether or not this distance increases (or decreases).

Furthermore, we find that the qualitative nature of the interactions is similar for both spheres and ellipsoids, and that varying the aspect ratio does not change the general tendencies of the locomotors, as was found by Ishikawa in [12] for models of interacting bacteria.

In future work, we plan to study more general stress distributions which consist of both polar and azimuthal components so that each swimmer rotates about its axis of motion while swimming in a particular direction, which is the case for microorganisms such as *V. carteri*. We also plan to investigate time-dependent stress distributions, as well as the collective swimming behavior of many locomotors.

An important question that is left open by both our work and by that of others, is what constitutes an appropriate biophysically-based model for the motive stress or slip velocity used to propel the model organism. For a true organism such as *V. carteri*, it is most likely an inter-leaved combination of applied stress imparted by the "rowing flagellae", and a no-slip condition along their supporting surface. An important modeling task is to develop appropriately coarse-grained boundary conditions that capture such combinations, the constituents of which possibly being strongly dynamical and responsive to external flows.

Acknowledgments

The work of A.K., M.J.S., and A.K.T. is supported by NSF Grant DMS-0412203 and DOE Grant DE-FG02-88ER25053. A.K.T. is a Royal Swedish Academy of Sciences Research Fellow supported by a grant from the Knut and Alice Wallenberg Foundation, and acknowledges this support as well as support from an Alfred P. Sloan Research Fellowship. We thank R. Goldstein, D. Saintillan, and S. Spagnolie for useful conversations, and the Aspen Center for Physics, where some of this work was done, for its hospitality.

Appendix A

A.1. One sphere: analytic solution

In this section, we derive the exact axisymmetric solution for a single locomoting (unit) sphere with a prescribed tangential surface stress distribution. The derived solution is in the reference frame of the body (sphere) and is based on spherical coordinates and spherical harmonics. Note that v is the fluid viscosity.

Consider a sphere centered at the origin and of radius one. The coordinates are (r, θ, ϕ) corresponding to the radius, the polar angle and the azimuthal angle in the spherical coordinate reference frame. We seek an axisymmetric solution to the Stokes equations for the flow which has specified tangential stress on the sphere along lines of constant angle ϕ:

$$\nabla \cdot \boldsymbol{\sigma} = \mathbf{0}, \quad \nabla \cdot \mathbf{u} = 0, \tag{19}$$

$$\sigma = -p\mathbf{I} + 2v\mathbf{E}, \tag{20}$$

$$\left(\mathbf{I} - \mathbf{e}_n \mathbf{e}_n^T\right)\boldsymbol{\sigma}\mathbf{e}_n = f\hat{\boldsymbol{\theta}}. \tag{21}$$

We seek the solution through the Stokes stream function $\psi(r, \theta)$. First, let us define u as the magnitude of the normal component of velocity, and v as the magnitude of the tangential component of velocity: $(u, v) = (\mathbf{u} \cdot \hat{\mathbf{r}}, \mathbf{u} \cdot \hat{\boldsymbol{\theta}})$

$$u = \frac{1}{r^2 \sin\theta}\frac{\partial \psi}{\partial \theta} = \frac{-1}{r^2}\frac{\partial \psi}{\partial \mu}, \tag{22}$$

$$v = \frac{-1}{r \sin\theta}\frac{\partial \psi}{\partial r} = \frac{-1}{r\sqrt{1-\mu^2}}\frac{\partial \psi}{\partial r}, \tag{23}$$

where $\mu = \cos\theta$. Note that

$$\hat{\mathbf{r}} = (\cos\phi \sin\theta, \sin\phi \sin\theta, \cos\theta),$$

$$\hat{\boldsymbol{\theta}} = (\cos\phi \cos\theta, \sin\phi \cos\theta, -\sin\theta).$$

Taking the curl of the momentum equation (Eq. (19)) gives

$$\Delta\boldsymbol{\omega} = 0, \tag{24}$$

where the vorticity $\boldsymbol{\omega} = \nabla \times \mathbf{u}$. It can be shown that a consequence of this is that

$$\mathscr{L}^2\psi = 0, \quad \mathscr{L} = \partial_{rr} + \frac{\sin\theta}{r^2}\partial_\theta\left(\frac{1}{\sin\theta}\partial_\theta\right) = \partial_{rr} + \frac{1-\mu^2}{r^2}\partial_{\mu\mu}. \tag{25}$$

We require that $\mathbf{u}$ be bounded at infinity and outside of the unit ball, for $r \gg 1$, that the velocity field be bounded at the poles $\mu = \pm 1$, and also require zero mass flux at infinity. Given these assumptions, the relevant stream function ψ may be expressed through an expansion of spherical harmonics R_n and Q_n themselves expressed in terms of Legendre polynomials P_n

$$\psi = a_1 Q_1 + \sum_{n\geqslant 1}\left(b_n + r^2\tilde{b}_n\right)R_n, \tag{26}$$

where

$$R_n(r,\mu) = \frac{-1}{n} r^{-n}(1-\mu^2)P_n'(\mu), \quad Q_1 = \frac{r^2}{2}(1-\mu^2).$$

Note that $P_0 = 1;\ P_1 = \mu;\ P_2 = \frac{1}{2}(3\mu^2 - 1)$.

In order to derive the coefficients $a_1,\ b_n$ and $\tilde{b}_n (n \geqslant 1)$, we will apply a set of three boundary conditions and a zero net force condition.

(1) We assume uniform flow at infinity with speed U in the negative-z direction ($\mathbf{u}|_\infty = -U\hat{\mathbf{k}}$ in Cartesian coordinates). Therefore, $a_1 = -U$, and the stream function becomes

$$\psi = -\frac{1}{2}Ur^2(1-\mu^2) + \sum_{n\geqslant 1}(b_n + r^2\tilde{b}_n)R_n. \tag{27}$$

(2) We apply the no penetration condition $u|_{r=1} = 0$ (normal component of velocity is zero)

$$u|_{r=1} = -U\mu - \sum_{n\geqslant 1}(b_n + \tilde{b}_n)(n+1)P_n(\mu) = 0, \tag{28}$$

requiring that

$$b_1 + \tilde{b}_1 = -\frac{U}{2}, \tag{29}$$

$$b_n + \tilde{b}_n = 0, n \geqslant 2. \tag{30}$$

(3) Next, we apply the stress condition $2\nu E_{r\theta}|_{r=1} = f_\theta$. For an axisymmetric flow we will have

$$\frac{f_\theta}{2\nu} = e_{r\theta}|_{r=1} = \frac{r}{2}\frac{\partial}{\partial r}\left(\frac{v}{r}\right)|_{r=1} = \frac{1}{2\sqrt{1-\mu^2}}\frac{\partial}{\partial r}\left(\frac{-1}{r^2}\frac{\partial\psi}{\partial r}\right)\Big|_{r=1} \tag{31}$$

$$= \frac{-1}{2\sqrt{1-\mu^2}}(\psi_{rr} - 2\psi_r)|_{r=1} \tag{32}$$

where

$$\psi_r|_{r=1} = -\frac{1}{2}U(1-\mu^2) + 2\sum_{n\geqslant 1}\frac{b_n}{n}(1-\mu^2)P_n'(\mu), \tag{33}$$

$$\psi_{rr}|_{r=1} = -U(1-\mu^2) - \sum_{n\geqslant 1}\frac{b_n}{n}[4n-2](1-\mu^2)P_n'(\mu). \tag{34}$$

We assume that the tangential stress distribution is a smooth function given by

$$\sigma_{r\theta} = f_\theta = -f_0\sqrt{1-\mu^2}\sum_{m\geqslant 0}\alpha_m P_m(\mu), \tag{35}$$

where f_0 is a constant. Note that the solution constructed by Short et al. [25] is for the case when f_θ is a constant. Eq. (32) becomes

$$\frac{f_0}{\nu}(1-\mu^2)\sum_{m\geqslant 0}\alpha_m P_m(\mu) = -4\sum_{n\geqslant 1}\frac{b_n}{n}[n+1/2](1-\mu^2)P_n'(\mu). \tag{36}$$

Now we integrate this equation against P_k', and use the identities

$$(1-\mu^2)P_n'(\mu) = \frac{n(n+1)}{2n+1}(P_{n-1}(\mu) - P_{n+1}(\mu)), \tag{37}$$

$$\int_{-1}^{1} P_k(\mu)P_n(\mu)d\mu = \frac{2}{2k+1}\delta_{n,k}, \tag{38}$$

and

$$\int_{-1}^{1} P_k'(\mu)(1-\mu^2)P_n'(\mu)d\mu = -\int_{-1}^{1} P_k(\mu)\left((1-\mu^2)P_n'(\mu)\right)'d\mu = \frac{k(k+1)}{k+1/2}\delta_{n,k}. \tag{39}$$

Therefore,

$$b_n = \frac{f_0 n}{2\nu(2n+1)}\left(\frac{\alpha_{n+1}}{2n+3} - \frac{\alpha_{n-1}}{2n-1}\right), \quad n \geqslant 1. \tag{40}$$

We proceed by working out the trivial case for which $\alpha_0 = 1$ and $\alpha_m = 0,\ m > 0$, resulting in

$$b_1 = -\frac{f_0}{6\nu}, \tag{41}$$

$$b_n = 0, n \geqslant 2. \tag{42}$$

(4) Finally, we require the net force to be zero. In order to enforce this condition, we must first compute the pressure, p, and also the rate-of-strain component e_{rr}. We dot the Stokes equation (Eq. (19)) with $\hat{\mathbf{r}}$ and come up with an equation for the r-derivative of the pressure:

$$\frac{1}{\nu}\frac{\partial p}{\partial r} = \hat{\mathbf{r}} \cdot (\nabla^2 \mathbf{u}) = \frac{2\mu}{r^4}\psi_{\mu\mu} - \frac{1}{r^2}\psi_{\mu rr} = \frac{4\mu}{r^3}\tilde{b}_1. \tag{43}$$

Therefore,

$$\frac{\partial p}{\partial r} = \frac{4\nu\mu}{r^3}\tilde{b}_1. \tag{44}$$

We integrate Eq. (44) with respect to r and find that

$$p(r,\mu) = G(\mu) - \frac{2\nu\mu}{r^2}\tilde{b}_1 + C_1, \tag{45}$$

where C_1 is a constant and G is only a function of μ. Since the pressure is required to be harmonic, i.e. $\nabla^2 p(r,\mu) = 0$, we set $G(\mu) = 0$ in order for the pressure to be finite at the poles ($G(\mu)$ is the solution to the differential equation $\frac{dG}{d\mu} = \frac{C}{1-\mu^2}$), giving us

$$p(r,\mu) = -\frac{2\nu\mu}{r^2}\tilde{b}_1 + C_1. \tag{46}$$

The rate-of-strain e_{rr} is given as

$$e_{rr} = \frac{\partial u}{\partial r} = \frac{2}{r^3}\psi_\mu - \frac{1}{r^2}\psi_{\mu r} = \frac{6\mu}{r^4}b_1 + \frac{2\mu}{r^2}\tilde{b}_1. \tag{47}$$

Now we have all the pieces necessary to write down the stress $\vec{t} = \boldsymbol{\sigma}\vec{n}$. In polar coordinates, with only the rate-of-strain components e_{rr} and $e_{\theta r}$ needed to do this

$$\vec{t} = T_{rr}\hat{r} + T_{\theta r}\hat{\theta} = \begin{pmatrix} -p + 2\nu e_{rr} \\ 2\nu e_{\theta r} \end{pmatrix} = \begin{pmatrix} 12\nu\mu b_1 + 6\nu\mu\tilde{b}_1 + C_1 \\ -f_0\sqrt{1-\mu^2} \end{pmatrix}. \tag{48}$$

We may now find the net force in any direction.

$$F_x = F_y = \oint \vec{t}\cdot\vec{e}_x dS = \oint [\cos\phi \sin(\theta) T_{rr} + \cos\phi\cos(\theta)T_{\theta r}]dS. \tag{49}$$

$$F_z = \oint \vec{t}\cdot\vec{e}_z dS = \oint [T_{rr}\cos\theta - T_{\theta r}\sin\theta]dS. \tag{50}$$

There is a $\cos\phi$ term sitting inside the F_x and F_y integrals, so both F_x and F_y are zero. We require F_z to also be zero:

$$\begin{aligned} 0 = F_z &= \int_0^{2\pi}\int_0^{\pi} [T_{rr}\cos\theta - T_{\theta r}\sin\theta]\sin\theta d\theta d\phi = \int_0^{2\pi}\int_{-1}^{1} [T_{rr}\mu - T_{\theta r}\sqrt{1-\mu^2}]d\mu d\phi \\ &= 2\pi[4\nu\mu^3 b_1 + 2\nu\mu^3\tilde{b}_1 + C_1\mu^2/2 + f_0(\mu - \mu^3/3)]_{-1}^{1}. \end{aligned} \tag{51}$$

Therefore,

$$0 = 2b_1 + \tilde{b}_1 + \frac{f_0}{3\nu}. \tag{52}$$

We now write the system of three equations and unknowns that comes out of all the above conditions, and solve for the three unknowns, $b_1,\ \tilde{b}_1$ and U:

$$\begin{pmatrix} 1/2 & 1 & 1 \\ 0 & 2 & 1 \\ 0 & 1 & 0 \end{pmatrix}\begin{pmatrix} U \\ b_1 \\ \tilde{b}_1 \end{pmatrix} = \begin{pmatrix} 0 \\ -\frac{f_0}{3\nu} \\ -\frac{f_0}{6\nu} \end{pmatrix} \tag{53}$$

giving us

$$\begin{pmatrix} U \\ b_1 \\ \tilde{b}_1 \end{pmatrix} = \begin{pmatrix} \frac{f_0}{3v} \\ -\frac{f_0}{6v} \\ 0 \end{pmatrix} \tag{54}$$

Note that $b_n = \tilde{b}_n = 0$ $n \geqslant 2$. The stream function becomes

$$\psi = -\frac{f_0}{6v}\left(r^2 - \frac{1}{r}\right)(1-\mu^2) \tag{55}$$

for the stress distribution $\sigma_{r\theta} = f_\theta = -f_0\sqrt{1-\mu^2}$. The tangential velocity v (normal velocity u is zero in reference frame of body) may be computed from the stream function using Eq. (23).

Appendix B

B.1. One prolate ellipsoid: analytic solution

In this section, we derive the exact axisymmetric solution for a single locomoting ellipsoid with a prescribed tangential surface stress distribution. The derived solution is in the reference frame of the body (ellipsoid) and is based on ellipsoidal coordinates and ellipsoidal harmonics. Note that v is the fluid viscosity.

Consider an ellipsoid centered at the origin. The coordinates are (Γ, μ, ϕ) corresponding to the ratio of major axis length to distance between the foci, the cosine of the polar angle, and the azimuthal angle in the prolate spheroidal coordinate reference frame. The relation between Cartesian and prolate spheroidal systems is the following:

$$(x, y, z) = (\omega\cos\phi, \omega\sin\phi, k\cos\theta\cosh\eta = k\mu\Gamma), \tag{56}$$

where $\omega = k\sin\theta\sinh\eta$. $\Gamma = \Gamma_0 > 1$ is a confocal ellipsoid with foci $(0, 0, \pm k)$, $1 \leqslant \Gamma \leqslant \infty$, $-1 \leqslant \mu \leqslant 1$.

We seek an axisymmetric solution to the Stokes equations (Eq. (19)) for the flow which has specified tangential stress on the ellipsoid along lines of constant angle ϕ through the Stokes stream function $\psi(\Gamma, \mu)$. Just as for the case of the sphere, it can be shown that ψ must satisfy

$$\mathscr{L}^2\psi = 0, \ \mathscr{L} = \frac{1}{k^2(\mu^2 - \Gamma^2)}[(1-\Gamma^2)\partial_{\Gamma\Gamma} - (1-\mu^2)\partial_{\mu\mu}] \tag{57}$$

First, let us define u as the magnitude of the normal component of velocity, and v as the magnitude of the tangential component of velocity: $(u, v) = (\mathbf{u}\cdot\hat{\mathbf{\Gamma}}, \mathbf{u}\cdot\hat{\boldsymbol{\mu}})$

$$u = \frac{1}{k^2\sqrt{\Gamma^2-\mu^2}\sqrt{\Gamma^2-1}}\frac{\partial\psi}{\partial\mu}, \tag{58}$$

$$v = \frac{-1}{k^2\sqrt{\Gamma^2-\mu^2}\sqrt{1-\mu^2}}\frac{\partial\psi}{\partial\Gamma}. \tag{59}$$

Note that

$$\hat{\mathbf{\Gamma}} = \left(\frac{\Gamma(1-\mu^2)^{1/2}}{(\Gamma^2-\mu^2)^{1/2}}\cos\phi, \frac{\Gamma(1-\mu^2)^{1/2}}{(\Gamma^2-\mu^2)^{1/2}}\sin\phi, \frac{\mu(\Gamma^2-1)^{1/2}}{(\Gamma^2-\mu^2)^{1/2}}\right),$$

$$\hat{\boldsymbol{\mu}} = \left(\frac{\mu(\Gamma^2-1)^{1/2}}{(\Gamma^2-\mu^2)^{1/2}}\cos\phi, \frac{\mu(\Gamma^2-1)^{1/2}}{(\Gamma^2-\mu^2)^{1/2}}\sin\phi, -\frac{\Gamma(1-\mu^2)^{1/2}}{(\Gamma^2-\mu^2)^{1/2}}\right).$$

The stream function ψ may be expressed through an expansion of ellipsoidal harmonics R_n and S_n, themselves expressed in terms of the Legendre polynomials of the first kind P_n and the Legendre polynomials of the second kind Q_n

$$\psi = a_1 R_1(\mu)R_1(\Gamma) + \sum_{n\geqslant 1}[b_n + \tilde{b}_n(\mu^2+\Gamma^2)]R_n(\mu)S_n(\Gamma), \tag{60}$$

where

$$R_n(x) = (1-x^2)P_n'(x),$$

$$S_n(x) = (1-x^2)Q_n'(x),$$

$$Q_n(x) = P_n(x)\int_x^\infty \frac{d\tau}{P_n^2(\tau)(\tau^2-1)}.$$

Note that $Q_n(x)$ include a log term, and that $Q_0(x) = \frac{1}{2}\ln\left(\frac{1+x}{1-x}\right)$, $Q_1(x) = \frac{x}{2}\ln\left(\frac{1+x}{1-x}\right) - 1$, and $Q_2(x) = \frac{3x^2-1}{4}\ln\left(\frac{1+x}{1-x}\right) - \frac{3x}{2}$. We also note that the form of ψ is analogous to the spherical case since $\mu^2 + \Gamma^2 - 1 = r^2$.

In order to derive the coefficients a_1, b_n and $\tilde{b}_n (n \geqslant 1)$, we will apply a set of three boundary conditions and a zero net force condition just as we did in the previous section for the sphere.

(1) We assume uniform flow at infinity with speed U in the negative-z direction ($\mathbf{u}|_\infty = -U\hat{\mathbf{k}}$ in Cartesian coordinates). Therefore, $a_1 = U/2$, and the stream function becomes

$$\psi = -\frac{U}{2}(1-\mu^2)(\Gamma^2-1) + \sum_{n\geqslant 1}[b_n + \tilde{b}_n(\mu^2+\Gamma^2)]R_n(\mu)S_n(\Gamma). \tag{61}$$

(2) We apply the no penetration condition $u|_{\Gamma=\Gamma_0} = 0$ (normal component of velocity is zero at the wall). Setting $u|_{\Gamma=\Gamma_0} = 0$ and dividing through by $1-\Gamma_0^2$ we get

$$0 = -U\mu + \sum_{n\geqslant 1} b_n[P_n(\mu)Q_n'(\Gamma_0)(-n)(n+1)] + \tilde{b}_n[P_n(\mu)Q_n'(\Gamma_0)(-n)(n+1)\left(\Gamma_0^2+\mu^2\right) + P_n'(\mu)Q_n'(\Gamma_0)(2\mu)(1-\mu^2)]. \tag{62}$$

(3) Next, we apply the stress condition $2ve_{\Gamma\mu}|_{\Gamma_0} = f_\theta$. We note that the scale factors (Lame coefficients) for the prolate ellipsoidal coordinate system are

$$h_1 = h_\Gamma = k\sqrt{\frac{\Gamma^2-\mu^2}{\Gamma^2-1}},$$
$$h_2 = h_\mu = k\sqrt{\frac{\Gamma^2-\mu^2}{1-\mu^2}},$$
$$h_3 = h_\phi = k\sqrt{\Gamma^2-1}\sqrt{1-\mu^2}.$$

For an axisymmetric flow we will have

$$\begin{aligned}\frac{f_\theta}{2v} = e_{\Gamma\mu}|_{\Gamma_0} = \frac{h_\mu}{2h_\Gamma}\frac{\partial}{\partial\Gamma}\left(\frac{v}{h_\mu}\right) + \frac{h_\Gamma}{2h_\mu}\frac{\partial}{\partial\mu}\left(\frac{u}{h_\Gamma}\right) = \frac{1}{2k^3}\Big(&\psi_\mu[2\mu(1-\mu^2)^{1/2}(\Gamma^2-1)^{-1/2}(\Gamma^2-\mu^2)^{-2}] \\ &+ \psi_\Gamma[2\Gamma(1-\mu^2)^{-1/2}(\Gamma^2-1)^{1/2}(\Gamma^2-\mu^2)^{-2}] + \psi_{\mu\mu}[(1-\mu^2)^{1/2}(\Gamma^2-1)^{-1/2}(\Gamma^2-\mu^2)^{-1}] \\ &+ \psi_{\Gamma\Gamma}[-(1-\mu^2)^{-1/2}(\Gamma^2-1)^{1/2}(\Gamma^2-\mu^2)^{-1}]\Big).\end{aligned} \tag{63}$$

As in the previous section, we assume that the tangential stress distribution is given by the function $f_\theta = -f_0\sqrt{1-\mu^2}$, where f_0 is a constant. The resulting equation is

$$\begin{aligned}-\frac{f_0k^3\left(\Gamma_0^2-\mu^2\right)^2}{2v\sqrt{\Gamma_0^2-1}} = \sum_{n\geqslant 1} &b_n[P_n'(\mu)Q_n'(\Gamma_0)(n)(n+1)(\Gamma_0^2-\mu^2)] + b_n[P_n(\mu)Q_n'(\Gamma_0)(n)(n+1)(\mu)] + b_n[P_n'(\mu)Q_n(\Gamma_0) \\ &\times(-n)(n+1)(\Gamma_0)] + \tilde{b}_n\left[P_n'(\mu)Q_n'(\Gamma_0)(n^2+n-1)\left(\Gamma_0^4-\mu^4\right)\right] \\ &+ \tilde{b}_n\left[P_n'(\mu)Q_n(\Gamma_0)(n)(n+1)(\Gamma_0)\left(\Gamma_0^2-3\mu^2\right)\right] + \tilde{b}_n\left[P_n(\mu)Q_n'(\Gamma_0)(n)(n+1)(\mu)\left(3\Gamma_0^2-\mu^2\right)\right].\end{aligned} \tag{64}$$

(4) Finally, we require the net force to be zero. In order to enforce this condition, we must first compute the pressure, p, and also the rate-of-strain component $e_{\Gamma\Gamma}$. We recall that the Stokes equation is

$$-\nabla p + v\nabla^2\mathbf{u} = 0, \tag{65}$$

where

$$\begin{aligned}\nabla p &= \left(\hat{\mathbf{e}}_1\frac{1}{h_1}\frac{\partial}{\partial\xi_1} + \hat{\mathbf{e}}_2\frac{1}{h_2}\frac{\partial}{\partial\xi_2} + \hat{\mathbf{e}}_3\frac{1}{h_3}\frac{\partial}{\partial\xi_3}\right)p = \left(\widehat{\mathbf{\Gamma}}\frac{1}{h_\Gamma}\frac{\partial}{\partial\Gamma} + \hat{\boldsymbol{\mu}}\frac{1}{h_\mu}\frac{\partial}{\partial\mu} + \hat{\boldsymbol{\phi}}\frac{1}{h_\phi}\frac{\partial}{\partial\phi}\right)p, \\ g_1 &= g_\Gamma = \frac{1}{h_1}, \quad g_2 = g_\mu = \frac{1}{h_2}, \quad g_3 = g_\phi = \frac{1}{h_3},\end{aligned} \tag{66}$$

the vector Laplacian dotted with $\widehat{\mathbf{\Gamma}}$ is (refer to [7])

$$\begin{aligned}\nabla^2\mathbf{u}\cdot\widehat{\mathbf{\Gamma}} &= \nabla^2u_1 - \frac{u_1}{g_1}\nabla^2g_1 + u_1\frac{\partial}{\partial\xi_1}\left(\nabla^2\xi_1\right) + u_2\frac{g_1}{g_2}\frac{\partial}{\partial\xi_1}(\nabla^2\xi_2) - 2g_2^2\frac{\partial g_1}{\partial\xi_2}\frac{\partial}{\partial\xi_1}\left(\frac{u_2}{g_2}\right) + 2g_1g_2\frac{\partial g_2}{\partial\xi_1}\frac{\partial}{\partial\xi_2}\left(\frac{u_2}{g_2}\right) \\ &= \nabla^2u - \frac{u}{g_\Gamma}\nabla^2g_\Gamma + u\frac{\partial}{\partial\Gamma}(\nabla^2\Gamma) + v\frac{g_\Gamma}{g_\mu}\frac{\partial}{\partial\Gamma}(\nabla^2\mu) - 2g_\mu^2\frac{\partial g_\Gamma}{\partial\mu}\frac{\partial}{\partial\Gamma}\left(\frac{v}{g_\mu}\right) + 2g_\Gamma g_\mu\frac{\partial g_\mu}{\partial\Gamma}\frac{\partial}{\partial\mu}\left(\frac{v}{g_\mu}\right),\end{aligned} \tag{67}$$

and the Laplacian operator is

$$\nabla^2 = g_1 g_2 g_3 \left[\frac{\partial}{\partial \xi_1} \left(\frac{g_1}{g_2 g_3} \frac{\partial}{\partial \xi_1} \right) + \frac{\partial}{\partial \xi_2} \left(\frac{g_2}{g_1 g_3} \frac{\partial}{\partial \xi_2} \right) + \frac{\partial}{\partial \xi_3} \left(\frac{g_3}{g_1 g_2} \frac{\partial}{\partial \xi_3} \right) \right]$$
$$= g_\Gamma g_\mu g_\phi \left[\frac{\partial}{\partial \Gamma} \left(\frac{g_\Gamma}{g_\mu g_\phi} \frac{\partial}{\partial \Gamma} \right) + \frac{\partial}{\partial \mu} \left(\frac{g_\mu}{g_\Gamma g_\phi} \frac{\partial}{\partial \mu} \right) + \frac{\partial}{\partial \phi} \left(\frac{g_\phi}{g_\Gamma g_\mu} \frac{\partial}{\partial \phi} \right) \right]. \tag{68}$$

We dot the Stokes equation with $\widehat{\mathbf{\Gamma}}$ to get

$$\frac{\partial p}{\partial \Gamma} = \nu h_\Gamma (\nabla^2 \mathbf{u} \cdot \widehat{\mathbf{\Gamma}}), \tag{69}$$

which comes out to be

$$\frac{\partial p}{\partial \Gamma} = \frac{\nu}{k^3} \Big[\psi_{\mu\mu} \{ -2\mu (\Gamma^2 - \mu^2)^{-2} \} + \psi_{\Gamma\Gamma} \{ 2\mu (\Gamma^2 - \mu^2)^{-2} \} + \psi_{\mu\mu\mu} \{ (1-\mu^2)(\Gamma^2 - 1)^{-1} (\Gamma^2 - \mu^2)^{-1} \}$$
$$+ \psi_{\mu\Gamma\Gamma} \{ (\Gamma^2 - 1)(\Gamma^2 - 1)^{-1} (\Gamma^2 - \mu^2)^{-1} \} \Big]. \tag{70}$$

We compute the rate-of-strain component $e_{\Gamma\Gamma}$ as

$$e_{\Gamma\Gamma} = \frac{1}{h_1} \frac{\partial u_1}{\partial \xi_1} + \frac{u_2}{h_1 h_2} \frac{\partial h_1}{\partial \xi_2} + \frac{u_3}{h_1 h_3} \frac{\partial h_1}{\partial \xi_3} = \frac{1}{h_\Gamma} \frac{\partial u}{\partial \Gamma} + \frac{v}{h_\Gamma h_\mu} \frac{\partial h_\Gamma}{\partial \mu}$$
$$= \frac{1}{k^3} \Big\{ \psi_\mu [-\Gamma (\Gamma^2 - \mu^2)^{-2} - \Gamma (\Gamma^2 - 1)^{-1} (\Gamma^2 - \mu^2)^{-1}] + \psi_\Gamma [\mu (\Gamma^2 - \mu^2)^{-2}] + \psi_{\mu\Gamma} [(\Gamma^2 - \mu^2)^{-1}] \Big\}. \tag{71}$$

Now we have all the pieces necessary to write down the stress $\vec{t} = \boldsymbol{\sigma} \vec{n}$. In polar coordinates, with only the rate-of-strain components $e_{\Gamma\Gamma}$ and $e_{\mu\Gamma}$ needed to do this, we see

$$\vec{t} = T_{\Gamma\Gamma} \widehat{\mathbf{\Gamma}} + T_{\mu\Gamma} \hat{\boldsymbol{\mu}} = \begin{pmatrix} -p + 2\nu e_{\Gamma\Gamma} \\ 2\nu e_{\mu\Gamma} \end{pmatrix}. \tag{72}$$

We may now find the net force in any direction.

$$F_x = F_y = \oint \vec{t} \cdot \vec{e}_x dS = \oint [\cos\phi \sin\theta^* T_{\Gamma\Gamma} + \cos\phi \cos\theta^* T_{\mu\Gamma}] dS. \tag{73}$$

$$F_z = \oint \vec{t} \cdot \vec{e}_z dS = \oint [T_{\Gamma\Gamma} \cos\theta^* - T_{\mu\Gamma} \sin\theta^*] dS, \tag{74}$$

where

$$\theta^* = \tan^{-1} \left[\frac{\Gamma}{\sqrt{\Gamma^2 - 1}} \tan\theta \right].$$

There is a $\cos\phi$ term sitting inside the F_x and F_y integrals, so both F_x and F_y are zero. We require F_z to also be zero:

$$0 = F_z = k^2 \int_0^{2\pi} \int_0^{\pi} [T_{\Gamma\Gamma} \cos\theta^* - T_{\mu\Gamma} \sin\theta^*] (\sin\theta) \sqrt{\Gamma_0^2 - \cos^2\theta} \sqrt{\Gamma_0^2 - 1} d\theta d\phi$$
$$= 2\pi k^2 \int_{-1}^{1} \left[T_{\Gamma\Gamma}(\mu) \left(\Gamma_0^2 - 1 \right) - T_{\mu\Gamma}(\Gamma_0) \sqrt{\Gamma_0^2 - 1} \sqrt{1 - \mu^2} \right] d\mu. \tag{75}$$

We divide through by $2\pi k^2 \left(\Gamma_0^2 - 1 \right)$ and rewrite this as

$$0 = \int_{-1}^{1} \left[T_{\Gamma\Gamma}(\mu) - T_{\mu\Gamma} \frac{\Gamma_0 \sqrt{1-\mu^2}}{\sqrt{\Gamma_0^2 - 1}} \right] d\mu = \int_{-1}^{1} \left[(-p + 2\nu e_{\Gamma\Gamma})(\mu) - (2\nu e_{\mu\Gamma}) \frac{\Gamma_0 \sqrt{1-\mu^2}}{\sqrt{\Gamma_0^2 - 1}} \right] d\mu$$
$$= \int_{-1}^{1} \left[\left(- \int_{\Gamma_0}^{\infty} \frac{\partial p}{\partial \Gamma} d\Gamma + 2\nu e_{\Gamma\Gamma} \right)(\mu) + \frac{f_0 \Gamma_0 (1-\mu^2)}{\sqrt{\Gamma_0^2 - 1}} \right] d\mu. \tag{76}$$

Thus, our final equation resulting from the net force condition is

$$- \int_{-1}^{1} \int_{\Gamma_0}^{\infty} \frac{\partial p}{\partial \Gamma}(\mu) d\Gamma d\mu + 2\nu \int_{-1}^{1} e_{\Gamma\Gamma}(\mu) d\mu = - \frac{4 f_0 \Gamma_0}{3 \sqrt{\Gamma_0^2 - 1}}. \tag{77}$$

Unlike the case of the single sphere, where we only had three unknowns, we now have $2N+1$ unknowns $b_1, b_2, \ldots b_N, \tilde{b}_1, \tilde{b}_2, \ldots \tilde{b}_N$, and U. We collocate the two boundary condition equations (Eqs. (62) and (64)) at the N points

on the surface of the ellipsoid, which along with the force equation (Eq. (77)) results in a system of $2N + 1$ equations. Note that we compute the coefficients for the force equations by integrating term by term, and that we may compute p by integrating $\frac{\partial p}{\partial \Gamma}$ (Eq. (70)) with respect to Γ.

References

[1] G.K. Batchelor, An Introduction to Fluid Dynamics, Cambridge University Press, 2000.
[2] H.C. Berg, Motile behavior of bacteria, Phys. Today 53 (2000) 24–29.
[3] J.R. Blake, A spherical envelope approach to ciliary propulsion, J. Fluid Mech. 46 (1971) 199–208.
[4] J.F. Brady, G. Bossis, Stokesian dynamics, Ann. Rev. Fluid Mech. 20 (1988) 111–157.
[5] L.J. Fauci, R. Dillon, Biofluidmechanics of reproduction, Ann. Rev. Fluid Mech. 38 (2006) 371–394.
[6] A.J. Goldman, R.G. Cox, H. Brenner, The slow motion of two arbitrarily oriented spheres through a viscous fluid, J. Chem. Eng. Sci. 21 (1966) 1151–1170.
[7] J. Happel, H. Brenner, Low Reynolds Number Hydrodynamics, Prentice-Hall, 1965.
[8] T. Ishikawa, M. Hota, Interaction of two swimming Paramecia, J. Exp. Biol. 209 (2006) 4452–4463.
[9] T. Ishikawa, T.J. Pedley, The rheology of a semi-dilute suspension of swimming model micro-organisms, J. Fluid Mech. 588 (2007) 399–435.
[10] T. Ishikawa, T.J. Pedley, Diffusion of swimming model micro-organisms in a semi-dilute suspension, J. Fluid Mech. 588 (2007) 437–462.
[11] T. Ishikawa, T.J. Pedley, T. Yamaguchi, Orientational relaxation time of bottom-heavy squirmers in a semi-dilute suspension, J. Theor. Biol. 249 (2007) 296–306.
[12] T. Ishikawa, G. Sekiya, Y. Imai, T. Yamaguchi, Hydrodynamic interactions between two swimming bacteria, Biophys. J. 93 (2007) 2217–2225.
[13] T. Ishikawa, M.P. Simmonds, T.J. Pedley, Hydrodynamic interaction of two swimming model micro-organisms, J. Fluid Mech. 568 (2006) 119–160.
[14] M.J. Lighthill, On the squirming motion of nearly spherical deformable bodies through liquids at very small Reynolds numbers, Commun. Pure Appl. Math. 5 (1952) 109–118.
[15] V. Magar, T. Goto, T.J. Pedley, Nutrient uptake by a self-propelled steady squirmer, Q. J. Mech. Appl. Math. 56 (2003) 65–91.
[16] V. Magar, T.J. Pedley, Average nutrient uptake by a self-propelled unsteady squirmer, J. Fluid Mech. 539 (2005) 93–112.
[17] W.F. Paxton, K.C. Kistler, C.C. Olmeda, A. Sen, S.K. St Angelo, Y. Cao, T.E. Mallouk, P.E. Lammert, V.H. Crespi, Catalytic nanomotors: autonomous movement of striped nanorods, J. Am. Chem. Soc. 126 (2004) 13424–13431.
[18] C.M. Pooley, G.P. Alexander, J.M. Yeomans, Hydrodynamic interaction between two swimmers at low Reynolds number, Phys. Rev. Lett. 99 (2007) 228103.
[19] C. Pozrikidis, Boundary Integral and Singularity Methods for Linearized Viscous Flow, Cambridge University Press, 1992.
[20] E.M. Purcell, Life at low Reynolds number, Am. J. Phys. 45 (1977) 3–11.
[21] Y. Saad, Iterative Methods for Sparse Linear Systems, PWS Publishing Co., 1996.
[22] D. Saintillan, E. Darve, E.S.G. Shaqfeh, A smooth particle-mesh Ewald algorithm for Stokes suspension simulations: the sedimentation of fibers, Phys. Fluids 17 (2005) 033301.
[23] D. Saintillan, M.J. Shelley, Orientational order and instabilities in suspensions of self-locomoting rods, Phys. Rev. Lett. 99 (2007) 058102.
[24] M.J. Shelley, A.K. Tornberg, Microstrucural dynamics in complex fluids, in: M. Bazant (Ed.), Handbook in Materials Modeling, Kluwer Academic Publishers, 2005.
[25] M.B. Short, C.A. Solari, S. Ganguly, T.R. Powers, J.O. Kessler, R.E. Goldstein, Flows driven by flagella of multicellular organisms enhance long-range molecular transport, PNAS 103 (2006) 8315–8319.
[26] A. Sidi, Application of class S_m variable transformations to numerical integration over surfaces of spheres, J. Comput. Appl. Math. 184 (2005) 475–492.
[27] R.A. Simha, S. Ramaswamy, Hydrodynamic fluctuations and instabilities in ordered suspensions of self-propelled particles, Phys. Rev. Lett. 89 (2002) 058101.
[28] C.A. Solari, S. Ganguly, J.O. Kessler, R.E. Michod, R.E. Goldstein, Multicellularity and the functional interdependence of motility and molecular transport, PNAS 103 (2006) 1353–1358.
[29] M. Stimson, G.B. Jeffrey, Proc. Roy. Soc. A 111 (1926) 110.
[30] A.K. Tornberg, Numerical simulations of the dynamics of fiber suspensions, in: Multiscale Methods in Science and Engineering, Lecture Notes in Computational Science and Engineering, Springer-Verlag, 2005.
[31] A.K. Tornberg, K. Gustavsson, A numerical method for simulations of rigid fiber suspensions, J. Comput. Phys. 215 (2006) 172–196.
[32] A.K. Tornberg, M.J. Shelley, Simulating the dynamics and interactions of flexible fibers in Stokes flow, J. Comput. Phys. 196 (2004) 8–40.